AD-A080 220 UNITED TECHNOLOGIES CORP SUNNYVALE CALIF CHEMICAL SY--ETC F/G 21/8.2
ROTATING VALVE FOR VELOCITY COUPLED COMBUSTION RESPONSE MEASURE--ETC(U)
NOV 79 R S BROWN, R C WAUGH F49620-77-C-0048
UNCLASSIFIED CSD-2624-FR AFOSR-TR-80-0055 NL

1 OF 1
AD A080220

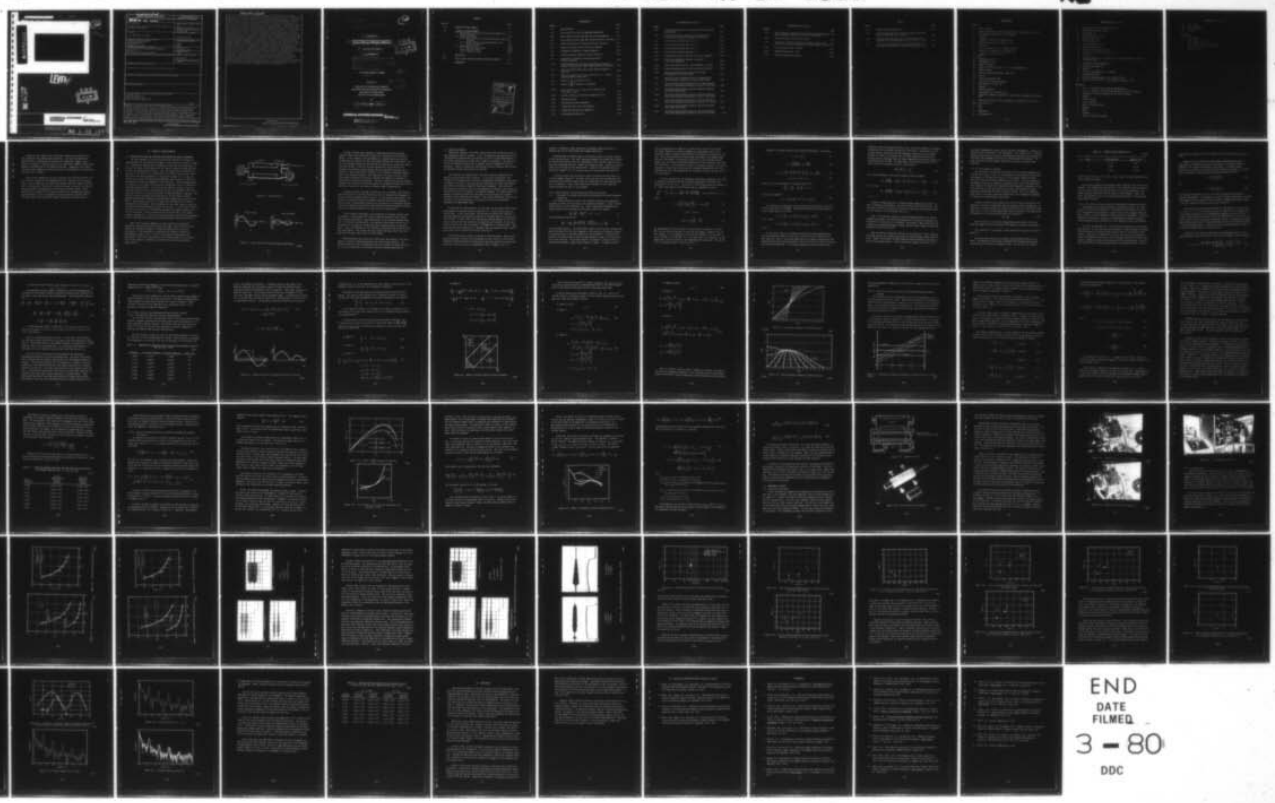

END
DATE FILMED
3-80
DDC

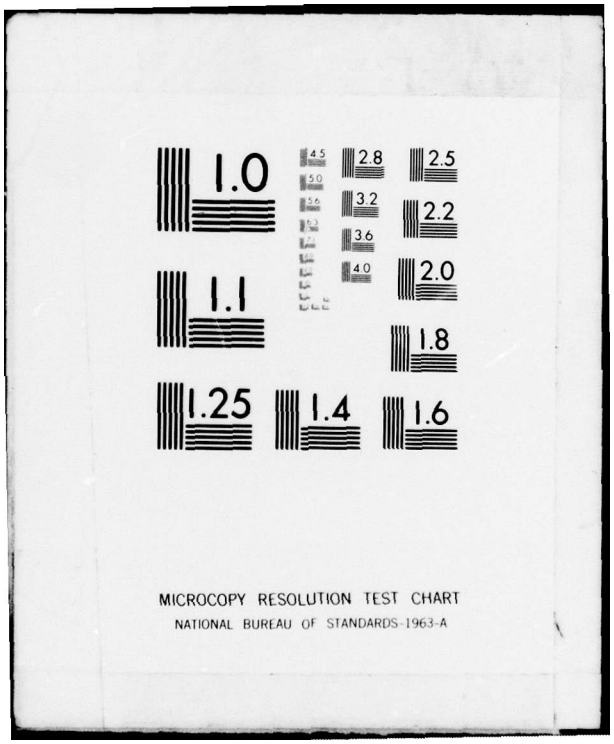
1.0
1.1
1.25
1.4
1.6
1.8
2.0
2.2
2.5
2.8
3.2
3.6
4.0
4.5
5.0
5.6
MICROCOPY RESOLUTION TEST CHART
NATIONAL BUREAU OF STANDARDS-1963-A

LEVEL III

CHEMICAL SYSTEMS DIVISION
UNITED TECHNOLOGIES

SECURITY CLASSIFICATION OF THIS PAGE (When Data Entered) Unclassified

REPORT DOCUMENTATION PAGE

READ INSTRUCTIONS BEFORE COMPLETING FORM

1. REPORT NUMBER AFOSR-TR- 80-0055	2. GOVT ACCESSION NO. / 3. RECIPIENT'S CATALOG NUMBER
4. TITLE (and Subtitle) ROTATING VALVE FOR VELOCITY COUPLED COMBUSTION RESPONSE MEASUREMENTS	5. TYPE OF REPORT & PERIOD COVERED FINAL 1 Jan 77 - 30 Sep 79
	6. PERFORMING ORG. REPORT NUMBER CSD 2624-FR
7. AUTHOR(s) R S BROWN AND R C WAUGH	8. CONTRACT OR GRANT NUMBER(s) F49620-77-C-0048
9. PERFORMING ORGANIZATION NAME AND ADDRESS CHEMICAL SYSTEMS DIVISION UNITED TECHNOLOGIES P O BOX 358 SUNNYVALE, CA 94088	10. PROGRAM ELEMENT, PROJECT, TASK AREA & WORK UNIT NUMBERS 2308A1 61102F
11. CONTROLLING OFFICE NAME AND ADDRESS AIR FORCE OFFICE OF SCIENTIFIC RESEARCH/NA BUILDING 410 BOLLING AIR FORCE BASE DC 20332	12. REPORT DATE 30 November 1979 / 13. NUMBER OF PAGES 40
14. MONITORING AGENCY NAME & ADDRESS (if different from Controlling Office)	15. SECURITY CLASS. (of this report) UNCLASSIFIED / 15a. DECLASSIFICATION/DOWNGRADING SCHEDULE

16. DISTRIBUTION STATEMENT (of this Report)

Approved for public release; distribution unlimited.

17. DISTRIBUTION STATEMENT (of the abstract entered in Block 20, if different from Report)

18. SUPPLEMENTARY NOTES

19. KEY WORDS (Continue on reverse side if necessary and identify by block number)

ROTATING VALVE
COMBUSTION STABILITY
SOLID PROPELLANT COMBUSTION

20. ABSTRACT (Continue on reverse side if necessary and identify by block number)

CSD has investigated the dual valve approach for measuring propellant velocity coupled characteristics. Analytical studies have developed a mathematical analysis of the transient ballistics. The solution of the transient mass, momentum, and energy equations incorporates both linear and nonlinear velocity coupling, as well as pressure coupling, particle damping, flow turning, and nozzle losses in the analysis. The analysis shows that velocity coupling dominates the system response when the two valves operate 180 DEG out of the phase. The analytical solutions agree with known solutions for low frequency, bulk

over

DD FORM 1 JAN 73 1473

UNCLASSIFIED

SECURITY CLASSIFICATION OF THIS PAGE (When Data Entered)

Unclassified

mode conditions and for the frequency response characteristics at acoustic resonance. Studies were conducted to explore the limitations of the dual valve approach and to estimate the effects of experimental uncertainties. Parametric studies using the linear velocity coupling model indicated properties of the solution that suggested an approximate method for deriving the response from pressure data using the linear velocity coupling assumption. Parametric studies were also made using the nonlinear velocity coupling model. The results show the interaction of mean velocity magnitude, threshold velocity, and amplitude of the velocity oscillation on the predicted pressure oscillations. A method was developed to derive the velocity response from experimental data for a given threshold velocity, but no method was found for deriving threshold velocity from experimental data. Concurrently, an experimental apparatus was constructed and its performance under controlled cold-flow conditions compared with predictions. Agreement between predicted and experimental behavior was demonstrated under pressure-coupled conditions. In the velocity-coupled mode, the cold-flow tests showed control of the phase angle between the two valves is important to ensure proper performance of the apparatus. Apparatus improvements were made to achieve this control. Combustion tests were conducted on two nonaluminized propellants and on a propellant containing 21% aluminum. The apparatus performed satisfactorily and propellant velocity response data were obtained for all three propellants for frequencies between 150 Hz and 600 Hz. The results show reasonable reproductibility from test to test and the numerical values are reasonable compared to previously reported values obtained in the T-burner. Amplitude spectrum analyses of the pressure traces on the nonaluminized propellant show significant harmonic content. Since the area wave form contains very low harmonic content, this suggests that the nonlinear velocity coupling may provide a more realistic framework for data interpretation.

(12)

(18) AFOSR

(19) TR-80-0055

(14) CSD-2624-FR

(6) ROTATING VALVE FOR VELOCITY COUPLED COMBUSTION RESPONSE MEASUREMENTS.

(9) Final Scientific Report.

(11) November 1979

Contract No. F49620-77-C-0048

(15)

(12) 80

(16) 2308

(17) A1

Prepared for

DIRECTOR OF AEROSPACE SCIENCES
AIR FORCE OFFICE OF SCIENTIFIC RESEARCH
BOLLING AIR FORCE BASE
DISTRICT OF COLUMBIA 20332

by

(10) R. S. Brown and R. C. Waugh

CHEMICAL SYSTEMS DIVISION UNITED TECHNOLOGIES

391 927

JOB

CONTENTS

ILLUSTRATIONS

ILLUSTRATIONS (Continued)

ILLUSTRATIONS (Continued)

TABLES

NOMENCLATURE

Symbols

a	sonic velocity
A	acoustic admittance, combustion parameter in equations (19) and (20)
C	see equations (8) and (43), concentration
d	diameter
D	integration constant in equation (12)
E	integration constant in equation (12)
f	frequency
F	particle damping term ($\hat{F} = i\lambda C_m \hat{M}/(1+i\lambda\tau_d)$)
G	parameter in equations (45) through (46)
h( )	Heaviside unit step function
i	$\sqrt{-1}$
Im	imaginary part of ( )
k	see equation (10)
K( )	Kummers function
K_n	value of $\lvert\hat{\mu}_1/\hat{M}\rvert$ at Z_n for n = 1 or 4, see figure 2-9
L	chamber length
m	velocity coupling parameter, mass flux
M	Mach No.
M^*	defined by equation (26)
n	burning ratio pressure exponent
N	see equations (9) and (44)
p	pressure
q	chamber perimeter
Q	see equation (4), f/Δf of filter
r	transformed length in equation (7), burn rate in figures 2-32 through 2-40
R	response function, combustion parameter in equations (19) and (20)
Re( )	real part of ( )
S	area
t	time
T	temperature
T_k	see equation (5)

Y	see equations (6) and (38) through (42)
Z	dimensionless chamber length
Z_n	see figure 2-9
α	exponential growth rate
γ	specific heat ratio
Γ	time constant ratio
ϵ	acoustic pressure ($p/\gamma\bar{p}$)
$(\hat{\epsilon})^*$	complex conjugate of $\hat{\epsilon}$
λ	dimensionless frequency $2\pi fL/a$
λ_1	defined as solution of $\lambda_1(\lambda_1-1) = i\lambda\Gamma$
μ	viscosity
μ_n	Fourier coefficient in decomposition of nonlinear velocity coupling in equation (25)
ω	response of flame temperature
ψ	dimensionless area $S'/\bar{S}$
ρ	density
σ'	flow turning parameter ($\sigma' = M'd\bar{M}/dZ$)
τ	dimensionless time
τ_d	particle damping parameter ($\tau_d = \bar{a}d_p^2\rho_p/(18\mu L)$)
$\bar{X}_1$	value of Z at which $\bar{M} = 0$ and is given by $\bar{S}_{vo}/(\bar{S}_{vo} + \bar{S}_{v1})$

Subscripts

o	at Z = 0, constant part of Fourier decomposition
1	at Z = 1, component of Fourier decomposition at driver frequency
2	component of Fourier decomposition at double frequency
c	chamber
v	valve, velocity
b	burning surface
m	mass of condensed phase
d	damping
f	flame
r	resonant
p	particle, pressure coupling

FT	flow turning
DF	double frequency
TH	threshold

Superscripts

-	time average
o	zeroth order component
'	first order oscillating component
"	second order oscillating component
^	complex amplitude

1.0 INTRODUCTION AND SUMMARY

Coupling between the combustion process and the acoustics of the combustion chamber are important factors in determining combustion stability of a solid propellant rocket. This coupling results because the combustion process reacts to both the local acoustic pressure and the local acoustic velocity. Because of the complexity of both processes. they cannot be totally characterized analytically; therefore, laboratory test data are needed in making analytical combustion stability predictions. One attractive test method conceived by CSD is the rotating valve apparatus. CSD conducted two programs under AFRPL contract to develop and demonstrate the rotating valve method of measuring the pressure coupled combustion response of solid propellants. The results show agreement with T-burner measurements when the T-burner vent term is taken to be zero. In addition, reproducible operation of the apparatus has been demonstrated at pressures up to 1,500 psi with propellants containing as much as 18% aluminum.

The rotating valve apparatus also has the potential for measuring the velocity coupled response function of solid propellants. Velocity oscillations of controlled frequency and amplitude can be generated by simultaneously operating a rotating valve at each end of the motor, 180° out of phase. In this configuration, velocity coupling dominates, and the effects of other processes, such as pressure coupling, are minimized. With this modification, the rotating valve method offers the potential for experimentally and quantitatively investigating many characteristics of velocity coupling which have been postulated by purely analytical arguments. The nature of these characteristics determines the manner in which velocity coupling is incorporated into the overall combustion stability analysis of a solid propellant rocket motor; thus experimental evaluation of velocity coupling characteristics is essen tial.

Under AFOSR contract No.F49620-77-C-0048, CSD has investigated the dual valve approach for measuring velocity coupling characteristics. This investigation included:

A. Studies to analyze the transient ballistics and provide a method for data interpretation and analysis
B. Parametric studies to evaluate momentum effects and determine the frequency range for which valid data can be obtained
C. An error assessment of the methods used to reduce experimental data
D. The design and fabrication of experimental apparatus
E. Cold-flow studies to evaluate the performance of the apparatus and to develop methods for calibrating the apparatus for data reduction purposes
F. Combustion tests to evaluate the limits of the apparatus performance, to determine the ability to distinguish differences in velocity response functions, to study the effects of internal flow patterns on the derived velocity response, and to establish the applicability of the data analysis procedures.

Substantial progress was made towards developing the dual rotating valve. Analytical studies developed two models for the burner, one based on linear velocity coupling and the other based on nonlinear (or amplitude dependent) velocity coupling. Using one dimensional gas dynamics, these models also include the effects of pressure coupling, flow turning, and particle damping. These models predict the behavior of the burner to driving produced by two valves operating 180° out of phase, two valves operating in phase, and a single valve at either end of the motor. Comparisons show these models predict the proper behavior at low frequency, the proper system damping at the natural frequencies, and agree with the model for the modulated throat motor.

These models were then used to develop methods for deriving velocity response functions from experimental data. Reasonable accuracy was demonstrated for the linear velocity coupling model. For the nonlinear model, response functions can be derived if the threshold speed is known. Separating the threshold from the response, however, is extremely complex. Progress was made, but development of a useful data reduction procedure was not completed.

Cold-flow tests demonstrated satisfactory apparatus performance. Methods for calibrating the mechanical alignment were also verified in these tests.

Combustion tests demonstrated satisfactory apparatus performance with both aluminized and nonaluminized propellants. The data show reasonable reproducibility, significant differences with formulation changes, and an effect of frequency. Frequency spectra show significant harmonic content which appears to be generated by the combustion process. Comparisons with analytical predictions suggest the nonlinear velocity coupling model is qualitatively consistent with the data.

These results demonstrate the dual rotating valve technique warrants further study as a method for investigating velocity response of solid propellants. This is especially true when one considers the early stage of development of the apparatus, and the data reduction process, as well as the lack of sound mechanistic understanding of the velocity coupling process. These studies should evaluate the two combustion models for interpreting velocity coupling effects, should investigate the basic mechanism in greater detail, and should explore the correlation between laboratory and motor results.

2.0 TECHNICAL ACCOMPLISHMENTS

2.1 DESCRIPTION OF THE DUAL ROTATING VALVE METHOD FOR VELOCITY RESPONSE

The basic approach in the dual rotating valve method is to mount two rotating valves on the combustion chamber, one at each end, as shown in figure 2-1. Conventional nozzles are also mounted at each end of the test motor to control the steady state pressure and the location along the propellant grain at which the mean velocity is zero. Thus, the instantaneous nozzle area at each end of the motor may be represented by the sum of a steady state component and an oscillating component as indicated in figure 2-1. If the two valves are in phase, the oscillating components add, as shown in figure 2-2, producing an oscillating component in the total area. The resulting behavior is identical to the single rotating valve configuration which is dominated by pressure coupling effects. If the valves are 180° out of phase, the area oscillation produced by one valve exactly cancels that produced by the other valve and there is no net area oscillation to provide pressure coupling. Significant velocity oscillations are produced in the test motor, however, because the venting of combustion gas alternates between the two ends of the motor. These velocity oscillations couple with the combustion to produce burning rate oscillations. With a constant net vent area, these burning rate oscillations produce measurable pressure oscillations. These pressure oscillations can be related to the burning rate response by using a ballistic analysis of the burner. Thus, by operating the two valves 180° out of phase, velocity coupling can, in principle, be studied under conditions which maximize velocity coupling contributions and minimize pressure coupled contributions.

Eisel[1] and co-workers suggested a similar approach to generating controlled velocity oscillations several years ago. Their objective was to observe the luminosity response of aluminized propellants to velocity oscillations. Their experiment incorporated two identical choppers for modulating the exhaust flow. They did not, however, include additional conventional nozzles for independently controlling the mean flow environment nor did they attempt to measure and interpret the pressure oscillations quantitatively.

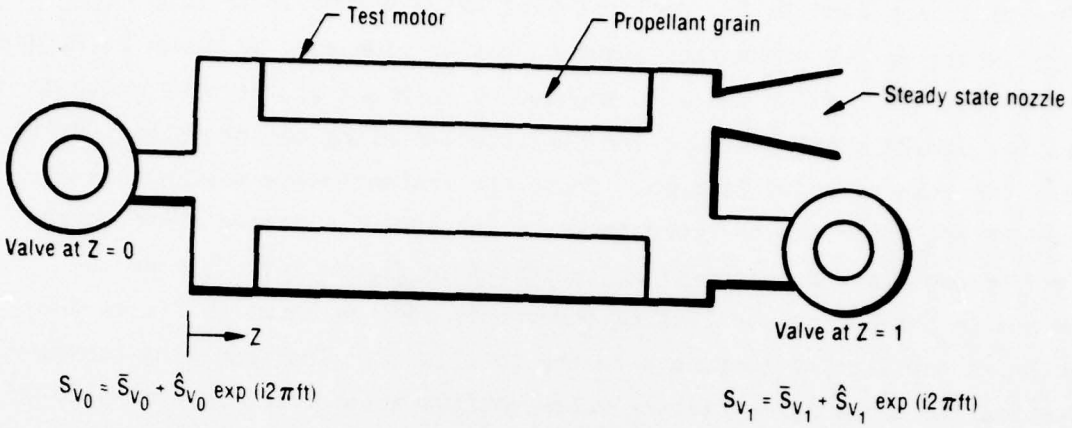

Figure 2-1. Valve Driving

08882R

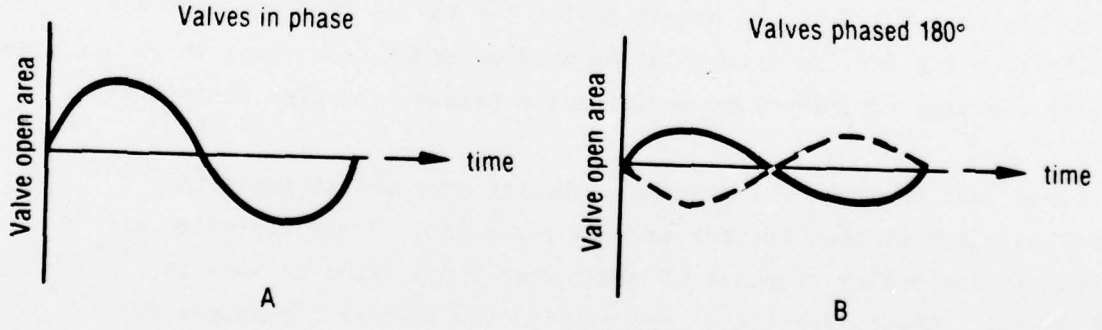

Figure 2-2. Valve Layout for Velocity Response Measurement

08883R

The dual rotating valve approach to measuring the velocity coupled response offers three potentially significant advantages over the T-burner method. In the T-burner, the test samples are located where both velocity oscillations and pressure oscillations produce burning rate oscillations. In fact, the maximum driving for the velocity oscillations is at best only 50% of the total driving. Since the T-burner measures the total burning rate response, the pressure coupled response must be subtracted from the total response to derive the velocity response. This requires independent measurement of the pressure response. More importantly, the uncertainties in the total measured response and pressure response add together to increase the uncertainty in the velocity response. The dual rotating valve method, however, maximizes the velocity driving and minimizes the pressure driving, which should improve the accuracy of the velocity response results significantly.

A second potential advantage involves the cost of testing. The T-burner method requires 10 to 20 tests at each condition of pressure and frequency to derive a velocity response function value. In the rotating valve method, only one test is required to obtain a response function value at each condition. There is also a corresponding reduction in the quantity of propellant required, which is an important consideration when several alternative propellant formulations are being considered for a particular motor application.

A third potential advantage is the capability for varying the mean flow environment. Current models for velocity coupling postulate that the mean flow environment may have a significant effect on the velocity response function. In the dual rotating valve, shifting mean nozzle area from one end of the burner to the other end changes the axial velocity profile in the test motor. Thus, the response can, in principle, be measured under different mean flow environments. The T-burner does not permit this easy control over the mean flow and hence cannot test for these effects.

These advantages offer potentially significant improvements in the measurement of velocity response properties over the T-burner approach. The studies described in the following sections were conducted to assess the utility of this new approach to quantitative velocity response measurements.

2.2 ANALYTICAL STUDIES

Theoretical analyses of the dual rotating valve were conducted as part of this program for several purposes. First, the magnitude and phase behavior of the oscillating pressure must be predicted to see if accurate measurements of the velocity response can be made over a range of frequencies. The sensitivity of the pressure oscillations to response function changes must also be estimated. Finally, a method for deriving the velocity response function from the measured pressure oscillations is required.

This requires two formulations of the basic ballistic equations which describe the oscillatory motor behavior. In the first formulation, the response of the burning rate to velocity oscillations and pressure oscillations is assumed to be known. The equations are formulated to predict the pressure and velocity oscillations based on these known responses. The solution of these equations provides a method for estimating the behavior of the burner and the sensitivity of this behavior to propellant changes. The second formulation assumes the pressure oscillations are known and the velocity and pressure responses of the propellant are unknown. This second formulation, which is the inverse of the first formulation, is required to derive the propellant responses from experimental data.

The analyses are complicated by the fact that two qualitative models have been proposed to describe velocity coupling [2,3,4], a linear model and a nonlinear model. In the linear model, the oscillatory burning rate responds to the local magnitude and direction (relative to the mean speed) of the velocity oscillations. In other words, the burning rate response depends on the direction of the mean gas flow as well as the magnitude and direction of the oscillating velocity, but does not depend on the magnitude of the mean speed. This model has been used extensively to interpret velocity coupled T-burner data,[5,6] motor data,[7] and in predictions of motor stability.[8]

The nonlinear model evolved by analogy to erosive burning. Erosive burning is postulated to result from increasing the heat transfer to the burning propellant surface produced by increasing the gas flow parallel to the surface. Analytical studies,[9] as well as experimental data,[10] suggest there is a

minimum, or threshold, speed which must be exceeded before the effect of parallel gas flow on the burning rate becomes significant.

Extrapolating a threshold speed to oscillatory flows is a central feature of the nonlinear model. The basic hypothesis assumes the burning rate responds to velocity oscillations when the instantaneous total velocity (mean velocity plus the oscillating velocity) exceeds the threshold speed. Analytical formulations which incorporate this concept were included in the Standard Stability Prediction Program[11] but the concepts have never been tested experimentally.

A critical review and evaluation of these two models was the subject of a recent JANNAF workshop.[12] The basic conclusion from this workshop was that both models have certain aspects which are reasonable, but other aspects which are not acceptable. Hence, both models were considered in the analytical studies conducted as part of this program.

2.2.1 Burner Analysis Incorporating Linear Velocity Coupling

2.2.1.1 Solutions for Pressure and Velocity Oscillations for Given Propellant Properties

The initial analytical studies were conducted using the one dimensional equations of motion for the gases in the combustion chamber, a linear velocity coupling model, and the ideal gas law. After linearizing the momentum and energy equations and retaining the oscillatory parts, one obtains:

$$\frac{\partial \epsilon'}{\partial Z} + \frac{\partial M'}{\partial \tau} + \frac{\partial(\bar{M} \cdot M')}{\partial Z} + \sigma' - F' = 0 \qquad (1)$$

for the momentum equation and

$$\frac{\partial \epsilon'}{\partial \tau} + \bar{M} \frac{\partial \epsilon'}{\partial Z} + \frac{\partial M'}{\partial Z} = \left(\frac{A_b qL}{S}\right)\epsilon' + \left(\frac{\bar{M}_b qL}{S}\right)(R_v + \omega_v) \frac{\bar{M} \cdot M'}{|\bar{M}|} \qquad (2)$$

for the energy equation. The factor $\bar{M}/|\bar{M}|$ arises in the velocity coupling term because the mass flow and flame temperature oscillations are assumed to depend on the oscillation in gas speed parallel to the propellant. A positive perturbation in velocity gives a positive perturbation in speed if the mean velocity is also positive. If the mean velocity is negative, a positive velocity perturbation produces a negative perturbation in speed. It should be noted

that these equations are identical to those used by Culick[13] to estimate the linear stability of acoustic chambers for longitudinal waves. The solutions, however, proceed along different paths because the objectives differ. Culick was interested in calculating the change in the complex eigenvalue for the chamber to determine the stability of self-excited acoustic waves; thus, his solution uses approximations which are valid only near resonant conditions. In this project, however, the primary interest is the burner response to driven flow oscillations at nonresonant frequencies; hence the approximations which are appropriate for resonant conditions are not valid in this development.

To obtain the solution for nonresonant conditions, equations 2 and 3 can be combined to eliminate dM'/dZ by assuming separation of variables and replacing $\partial(')/\partial\tau$ by $i\lambda(\hat{})$. The result is then differentiated with respect to Z. Terms containing M' and dM'/dZ can then be eliminated to yield

$$\frac{d^2\hat{\epsilon}}{dZ^2} - \left[\bar{M}\left(T_k + Q + \frac{2d\bar{M}}{dZ}\right) + Y\left(\frac{Q + d\bar{M}/dZ}{Q}\right)\right]\frac{d\hat{\epsilon}}{dZ} - T_k(Q + d\bar{M}/dZ)\,\hat{\epsilon} = 0 \quad (3)$$

where

$$Q \equiv i\lambda\left(\frac{1 + C_m + i\lambda\tau_d}{1 + i\lambda\tau_d}\right) + (1 - R_{FT})\frac{d\bar{M}}{dZ} \quad (4)$$

$$T_k \equiv i\lambda - A_b qL/S \quad (5)$$

$$Y \equiv \left(R_v + \omega_v\right)\frac{\bar{M}}{|\bar{M}|} \cdot \frac{d\bar{M}}{dZ} \quad (6)$$

Two approximations have been made in the derivation of equation 3. First, $\bar{M}^2 << 1$ which limits the analysis to low mean flow speeds. Second, $\bar{M}Y << Q$ has been assumed. If the magnitude of the velocity response is of the order of unity, then $\bar{M}Y$ is of order $\bar{M}^2$. Q, on the other hand, is of order $\bar{M}$. At high magnitudes of velocity response, this approximation breaks down. This point will be discussed further in section 2.2.2.3.

Equation 3 is second order and has variable coefficients. By letting

$$r \equiv (CZ - N)^2/C \tag{7}$$

$$C \equiv 0.5\left(\frac{d\bar{M}}{dZ}\right)\left(Q + T_k + \frac{2d\bar{M}}{dZ}\right) \tag{8}$$

$$N \equiv -0.5Y\left(\frac{Q + d\bar{M}/dZ}{Q}\right) + \frac{\bar{\chi}_1}{2}\ \frac{d\bar{M}}{dZ}\ \left(Q + T_k + 2\ \frac{d\bar{M}}{dZ}\right) \tag{9}$$

$$k \equiv T_k(Q + d\bar{M}/dZ)/(4C) \tag{10}$$

equation 3 can be transformed to a Kummers equation.[14]

$$r\ \frac{d^2\hat{\epsilon}}{dr^2} + \left(\frac{1}{2} - r\right)\ \frac{d\hat{\epsilon}}{dr} - k\hat{\epsilon} = 0 \tag{11}$$

The solution becomes[15]

$$\hat{\epsilon} = D\ K\ \left(k, \frac{1}{2}, r\right) + Er^{\frac{1}{2}}\ K\left\{k + \frac{1}{2}, \frac{3}{2}, r\right\} \tag{12}$$

The constants of integration can be evaluated from the nozzle flow equations at each end of the chamber. Assuming the nozzles and valves behave in a quasi-steady manner, one finds

$$\hat{M}_o = \bar{M}_o\left\{\hat{\psi}_o + 0.5\ (\hat{T}/\bar{T})_o\right\} = \bar{M}_o\ T_k\ \hat{\epsilon}_o - (d\hat{\epsilon}/dZ)_o \tag{13}$$

at Z = 0 and

$$\hat{M}_1 = \bar{M}_1\left\{\hat{\psi}_1 + 0.5\ (\hat{T}/\bar{T})_1\right\} = \bar{M}_1\ T_{k1}\hat{\epsilon}_1 - (d\hat{\epsilon}/dZ)_1 \tag{14}$$

at Z = 1.

At this point, there is a dilemma in relating the nozzle equations for the oscillating Mach number at each end of the burner to the values derived from equations 1 and 2. The nozzle equations are in terms of velocity and temperature oscillations whereas equations 1 and 2 are written in terms of velocity and pressure oscillations. If the flame temperature oscillation were known

separately from the burning rate oscillation, it would be possible to introduce an equation for the entropy oscillation in the burner. The solution to this entropy equation would yield the gas temperature oscillation at the nozzle entrance in terms of the pressure and the flame temperature oscillations. Without explicit knowledge about the flame temperature oscillation, however, an approximation must be made. Conventionally, the entropy oscillation at the nozzle entrance is assumed to be zero, which yields

$$\left(\frac{\gamma - 1}{\gamma}\right) \frac{\hat{P}}{\bar{P}} = \frac{1}{2} \frac{\hat{T}}{\bar{T}} \tag{15}$$

With this approximation, the nozzle boundary conditions become

$$Q\hat{M}_o = \left(\frac{-d\hat{\epsilon}}{dZ}\right)_o + \bar{M}_o T_{ko} \hat{\epsilon}_o = Q\bar{M}_o \left[0.5\hat{\epsilon}_o (\gamma - 1) + \hat{\psi}_o\right] \tag{16}$$

at Z = 0 and

$$Q\hat{M}_1 = \left(\frac{-d\hat{\epsilon}}{dZ}\right)_1 + \bar{M}_1 T_{k1} \hat{\epsilon}_1 = Q\bar{M}_1 \left[0.5\hat{\epsilon}_1 (\gamma - 1) + \hat{\psi}_1\right] \tag{17}$$

at Z = 1.

Because Y changes sign when the mean flow Mach number goes to zero, two sets of constants are required: one set for $0<Z<\bar{x}_1$ and one for $\bar{x}_1<Z<1$. The additional boundary conditions are obtained by requiring the oscillatory pressure and velocity to be continuous for $Z = \bar{x}_1$.

Thus, if the acoustic response, particle damping parameters and chamber dimensions are known, the oscillating components of pressure and velocity can be predicted for any point in the chamber. Furthermore, these predictions can be made for any phase relationship between the two values, simply by selecting appropriate values of $\hat{\psi}_0$ and $\hat{\psi}_1$.

There are several significant features to this solution. First, momentum and energy effects are included along with the transient mass balance contributions. Second, the analysis includes pressure coupled response, flow turning and particle damping effects. Third, the analysis permits the study of the

two-valve configurations as well as the one-valve configuration. Fourth, the analysis is not restricted to low frequencies. Thus, equation 12 is a general solution which should be valid for one-dimensional burners at all frequencies. This model was programmed in Fortran for the Burroughs 6700 computer. The basic definition for the Kummers function[15] was used to calculate these functions.

2.2.1.2 Verification of Solution

The solution of the equations described in the preceding paragraphs was verified in two ways. First, at low frequencies, the equations should reduce analytically to the equations derived for the pressure coupled rotating valve,[16,17] when the velocity response is set at zero. For low frequencies, the Kummers functions in equation 12 approach unity. With this simplification, equation 12 leads to the identical result reported in references 16 and 17 for the case of one valve and for both valves when operated in phase. Numerical calculations also yield identical results. This is an important point since it provides a numerical verification of the computer programming in addition to the analytical verification.

Second, this model should predict the correct acoustic damping when the combustor is driven at frequencies near the natural acoustic frequencies. In particular, one would expect the frequency difference at the half-power amplitudes (i.e., 0.707 x the peak amplitudes) would be related to the overall system damping of the self-excited system by the expression

$$\frac{\alpha}{f} = \frac{\pi \Delta f}{f} \qquad (18)$$

The left side can be evaluated independently from Culick's solutions while the right side can be evaluated from numerical solutions of the model.

This comparison has been made in three cases and the results are shown in table 2-1.

The first case contained only pressure coupling effects and used one valve. The second and third cases incorporated both pressure and velocity coupling, as well as particle damping effects. In case two, the response

TABLE 2-1. COMPUTED SYSTEM DAMPING (α/f)

T4126

Case	Culick Analysis	Equation (12)
1	0.112	0.117
2	0.155	0.156
3	0.102	0.108

functions were low (i.e., 0.2) while in case three, they were approximately an order of magnitude higher.

The excellent agreement found between these two methods substantiates the analysis. This demonstrates the analysis is not limited to the low frequency bulk flow conditions of the rotating valve, but is also applicable to the higher frequency conditions near the acoustic mode frequency. Thus, this model could provide a basis for interpreting data obtained in the modulated throat motor[18] as well.

2.2.1.3 Solutions for Velocity Response from Measured Pressure Oscillations

The analysis in the preceding section calculates $\hat{\epsilon}_o$ and $\hat{\epsilon}_1$, for input values of the propellant responses. In combustion tests however, $\hat{\epsilon}_o$ and $\hat{\epsilon}_1$ will be measured and a procedure is needed to derive the responses from the data. Efforts to obtain analytical solutions were not successful. Since the responses are implicit in equation 12, rearranging the forward solution to obtain expressions which are explicit in the response was also unsuccessful.

This left two alternatives: a trial and error approach, and an approximate solution. In the trial and error approach, one would assume the response value and estimate the expected magnitude and phase for the pressure oscillations. These would be compared to the data; new values for the response would be estimated; and new values for the pressure oscillations would be calculated. Attempts to apply this approach met with little success. The principal difficulty was in developing a method for estimating the new response

value from the comparison of the estimated and the observed pressure oscillations.

Attention was then directed to developing an approximate solution. A large number of numerical calculations were made to examine the predicted behavior of the pressure and velocity oscillations. To conduct these calculations, a method of selecting response functions was needed. A rational basis is provided by using thermal wave combustion models.[19,20,21]

$$R_p = \frac{n(1 + A - R)}{\lambda_1 + A/\lambda_1 - R} \tag{19}$$

and

$$R_v = \frac{m(1 + A - R)}{\lambda_1 + A/\lambda_1 - R} \tag{20}$$

The combustion parameters, A and R, can then be determined from pressure response measurements. The parameter, m, must be selected arbitrarily, although unity appears to give reasonable values, based on limited experimental values of velocity response functions from T-burner tests.[22,23]

Using values for the aluminized propellant, ANB 3066, (A = 15, $\underset{\sim}{R}$ = 4.97, n = 0.27, m = 1, Γ= 31.5) and the valves out of phase by 180°, a large number of calculations were run for the experimental geometry to be used in this study. These calculations showed that at low frequencies (i.e., λ= 0.75) the oscillating velocity is essentially spatially uniform. The magnitude is determined strictly by the size of the oscillating area of the two valves relative to the time-averaged area. In addition, the oscillating pressure is shown to be nearly a linear function of axial position.

Using the linear pressure observation, an approximate solution of the energy equation, which is explicit in the velocity response, can be developed.

$$(R_v + \omega_v) = \frac{T_k \hat{\epsilon}_o + \left(2T_k + d\bar{M}/dZ\right) \bar{x}_1 \left(\hat{\epsilon}_1 - \hat{\epsilon}_o\right) + \left(\hat{M}_1 - \hat{M}_o\right)}{(d\bar{M}/dZ)\ \hat{M}_1\ (1 - 2\bar{x}_1)} \tag{21}$$

The accuracy of this approximation has been examined numerically. The exact solution was used to predict oscillating pressures and velocities using estimated combustion parameters for ANB 3066. These pressures and velocities were then used to simulate experimental observations as inputs to equation 21. The velocity response derived from equation 21 was then compared with the original input value to determine the accuracy of the approximate solution. Figures 2-3 and 2-4 show comparisons of the derived and input velocity responses for a variety of conditions. This comparison was made using the imaginary part of the response since this is a parameter used in motor stability predictions.

The results in figure 2-3 were obtained by assuming the propellant contained no metal. With the valves phased by exactly 180°, the maximum error between the input and derived response is ±10% at the point where the response is a maximum. Allowing for phase misalignments of 3.5° between the two rotating valves, this error increases to ±20%. This error is typical for the experimental conditions and hence ±20% accuracy is expected for this procedure.

Figure 2-4 shows the effect of particle damping on the comparison between the exact and derived velocity response. These calculations were made by using the maximum particle damping at each frequency. Again, the agreement is better than ±10%. The approximate analysis, therefore, appears to provide a reasonably accurate solution at the lower frequencies for the conditions examined. This approximate solution also suggests a good method for estimating initial inputs if the complete trial and error analysis is ever required to improve the accuracy of the data reduction process.

2.2.1.4 Second Order Acoustic Analysis

Experimental studies, which are described in detail in section 2.3, showed significant generation of frequencies which are harmonics of the driven frequency. Since the waveform of the area oscillations has low harmonic content,[16] they must be generated by nonlinear burner acoustics or by nonlinear combustion processes. Therefore, an analysis was conducted to estimate the harmonic content produced by second order acoustics and linear velocity coupling.

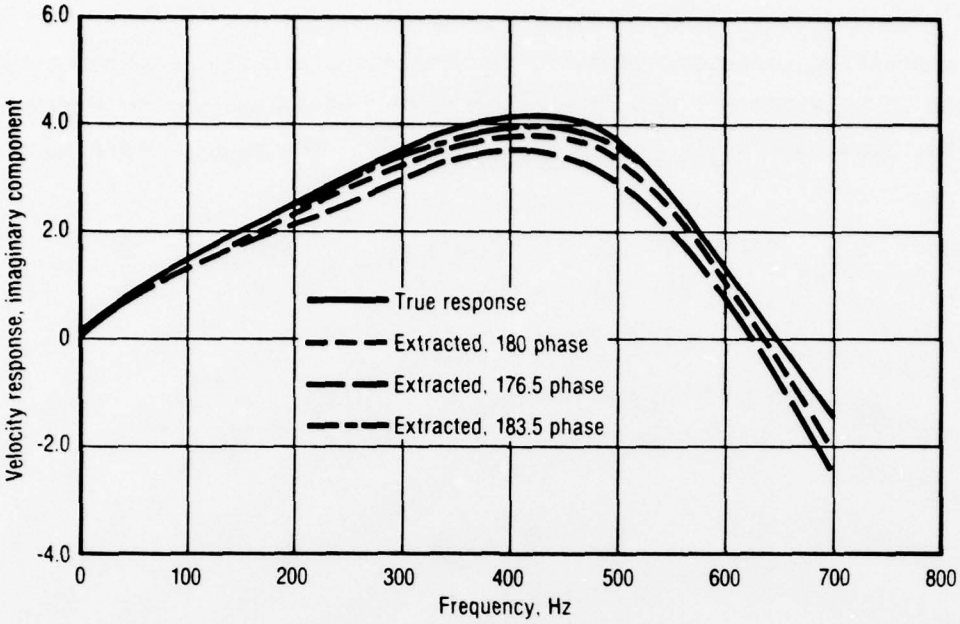

Figure 2-3. Error Analysis Study, ANB 3066 (No Particle-Damping)

12934

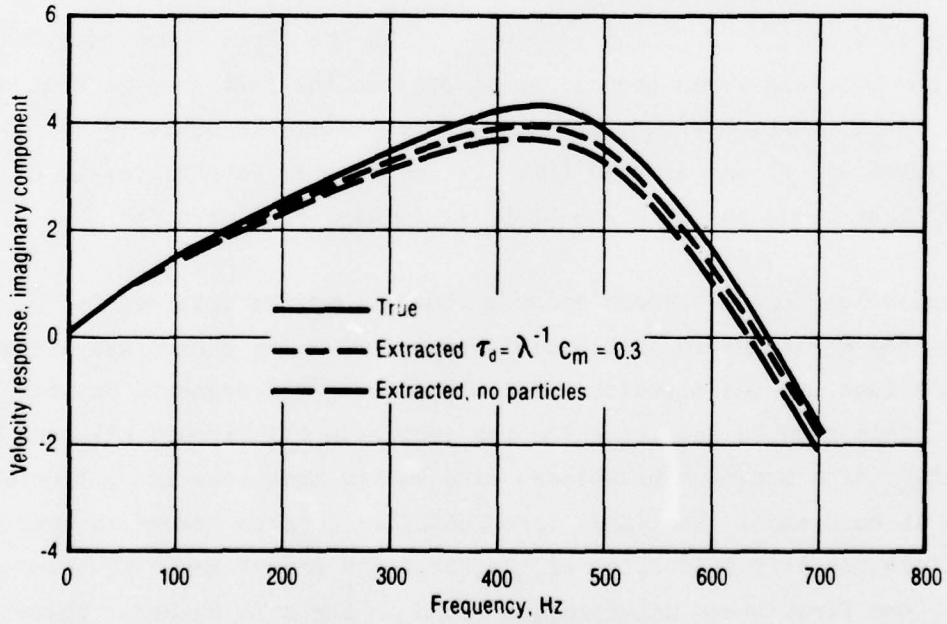

Figure 2-4. Error Analysis Study, ANB 3066 (Particle Effects Included)

12935

In this second order analysis, each variable is written in the form:

$$\epsilon = \epsilon^{o} + \epsilon' + \epsilon'' \tag{22}$$

By expressing velocity, density, burning rate, and flame temperature oscillations in this manner, separate conservation equations can be derived for the zeroth, first and second order perturbations. The second order equations are:

$$\frac{\partial \epsilon''}{\partial Z} + \frac{\partial M''}{\partial \tau} + \frac{\partial (M^{o} \cdot M'')}{\partial Z} + \frac{dM^{o}}{dZ} \cdot M'' = -\frac{1}{2} \frac{\partial (M')^{2}}{\partial Z} - \epsilon' \frac{\partial (M^{o} M')}{\partial Z} - \frac{dM^{o}}{dZ} \frac{m'_{b} M'}{m_{b}^{o}} \tag{23}$$

$$\frac{\partial \epsilon''}{\partial \tau} + \frac{\partial M''}{\partial Z} + \gamma \frac{\partial M^{o}}{\partial Z} \epsilon'' + M^{o} \frac{\partial \epsilon''}{\partial Z} - \frac{dM^{o}}{dZ} \left[\frac{T_{f}''}{T_{f}^{o}} + \frac{m_{b}''}{m_{b}^{o}} \right] = \tag{24}$$

$$-\gamma \epsilon' \frac{\partial M'}{\partial Z} - M' \frac{\partial \epsilon'}{\partial Z} + \frac{dM^{o}}{dZ} \frac{m'_{b}}{m^{o}_{b}} \frac{T_{f}'}{T_{f}^{o}}$$

In these equations, terms of order $(M^{o})^{2}$ have been neglected and the density perturbation is related to the pressure oscillation using the isentropic approximation.

There is a problem defining $\frac{T_{f}'}{T_{f}^{o}}$ and $\frac{m_{b}'}{m_{b}^{o}}$. In the first order equations, only the sum of these terms occurs, as it does on the left hand side of equation 24. These terms, however, also appear separately in equation 24. To separate $\frac{m_{b}'}{m_{b}^{o}}$ from $\frac{T_{f}'}{T_{f}^{o}}$ it was assumed that $\frac{T_{f}'}{T_{f}^{o}}$ is related isentropically to ϵ'. Corrected first order response function values were then used for $\frac{m_{b}'}{m_{b}^{o}}$.

The solution for the second order perturbations was obtained by expressing the equations in finite difference form. The burner was divided into 10 stations and the equations were written for the segments between the stations. This gave 20 equations for the variables ϵ''_{1} through ϵ''_{10} and M''_{1} through M''_{10} (nine momentum equations, nine energy equations and a boundary condition at each end). The first order solution is also needed at each station. Since the left hand sides of the first and second order equations are identical, the first order solution was found in the same manner. These values were then used in the right hand side of the second order solution. The product of two first order perturbations gives a steady component and a

component at double the frequency of the first order perturbation. Friedly[22] showed that if $\epsilon' = \mathrm{Re}\left[\hat{\epsilon}\ e^{i\omega t}\right]$ then

$$(\epsilon')^2 = 0.5\ \mathrm{Re}\left[(\hat{\epsilon})\ (\hat{\epsilon})^* + (\hat{\epsilon})^2 e^{i2\omega t}\right]$$

The results of this analysis for the same cases treated in the parametric study in section 2.2.2.2 are shown in table 2-2. The double frequency amplitudes produced by second order acoustics are clearly very small. Hence, nonlinear acoustics are not expected to be a significant factor in the generation of harmonic frequency components.

2.2.2 Burner Analysis Incorporating Nonlinear Velocity Coupling

2.2.2.1 Formulation of Nonlinear Velocity Coupling Model

The nonlinear velocity coupling model used in this analysis combines some kinematic concepts extrapolated from steady state erosive burning with a frequency dependent response function. This model, which has been studied by Price,[2,3] Culick[4] and Condon,[23] was developed by heuristic arguments to qualitatively explain some observed instabilities.

The basic approach assumes the velocity oscillations generate an oscillatory heat flux to the burning propellant surface. Since the heat flux depends on the magnitude of the velocity and not the direction, the oscillatory heat

TABLE 2-2. PRESSURE AMPLITUDES FOR LINEAR COUPLING WITH NONLINEAR ACOUSTICS, ANB 3066, $\tilde{\chi}_1 = 0.1256$

T6194

Frequency	At Driver Frequency	At Double Frequency	Ratio, dB
0.0598	0.616^{-2}	0.998^{-5}	-56
0.1197	0.484^{-2}	0.765^{-5}	-56
0.1795	0.438^{-2}	0.636^{-5}	-57
0.2394	0.412^{-2}	0.562^{-5}	-57
0.2992	0.372^{-2}	0.560^{-5}	-56
0.3590	0.298^{-2}	0.567^{-5}	-54
0.4189	0.206^{-2}	0.574^{-5}	-51

flux to the surface is rectified. A threshold speed is then added to the model by requiring the instantaneous speed to exceed the threshold before oscillatory effects are produced in the burning rate. These basic concepts are shown in figure 2-5. The driving velocity oscillation is compared in figure 2-5A to the mean velocity and the threshold speed. The "effective" velocity (i.e., the heat flux) is shown in figure 2-5B. Mathematically, this model can be formulated as follows. The effective oscillatory velocity can be written:

$$M^*h(M^*) = \bar{M}^*h(\bar{M}^*) + \mu_o + \mathrm{Re}\left[\hat{\mu}_1 e^{i\omega t}\right] + \mathrm{Re}\left[\hat{\mu}_2 e^{i2\omega t}\right] + \mathrm{Re}\left[\hat{\mu}_n e^{in\omega t}\right] \qquad (25)$$

where

$$M^* = \left|\bar{M} + \mathrm{Re}\left[\hat{M} e^{i\omega t}\right]\right| - M_{th} \qquad (26)$$

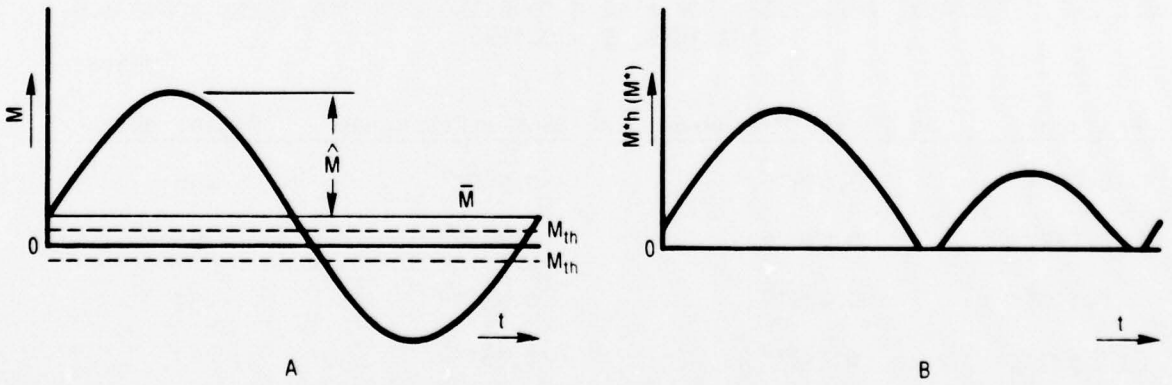

Figure 2-5. Effective Velocity for Nonlinear Velocity Coupling

21057

In equation 25, h( ) is the Heaviside unit step function, which is unity if the argument is positive and zero if the argument is negative.

The term $\bar{\mu}_1$ is the amplitude of the rectified wave at the driver frequency. This term is then combined with a "response function" to produce burning rate (and flame temperature) oscillations according to the equation

$$\frac{\hat{m}_b}{\bar{m}_b} + \frac{\hat{T}_f}{\bar{T}_f} = (R_p + \omega_p)\ \gamma\hat{\epsilon} + (R_v + \omega_v)\,\hat{\mu}_1 \qquad (27)$$

A more complete analysis of this model can be found in papers by Price and Dehority,[2,3] Culick,[4] and Condon,[23] and in the Standard Stability Prediction Program Manual.[11]

For given values of $\hat{M}$, $\bar{M}$ and M_{th} relatively simple expressions can be derived for $\hat{\mu}_1/\hat{M}$ which are valid for a particular domain of $\frac{|\hat{M}|}{M_{th}}$ and $\frac{|\bar{M}|}{M_{th}}$. Figure 2-6 shows a plot of $|\hat{M}|/M_{th}$ versus $|\bar{M}|/M_{th}$ in which four distinct regions are identified:

In region A:

$$\frac{\hat{\mu}_1}{\hat{M}} = 0 \qquad (|\bar{M}| + |\hat{M}| \leq M_{th}) \qquad (28)$$

In region B:

$$\frac{\hat{\mu}_1}{\hat{M}} = \frac{\bar{M}}{|\bar{M}|} \qquad (|\bar{M}| - |\hat{M}| > M_{th}) \qquad (29)$$

In region C:

$$\frac{\hat{\mu}_1}{\hat{M}} = \frac{2}{\pi|\hat{M}|}\left[(|\bar{M}| - M_{th})\cos\theta_1 + \frac{|\hat{M}|}{4}(\pi - 2\theta_1 + \sin(2\theta_1))\right]\frac{\bar{M}}{|\bar{M}|} \qquad (30)$$

$$\text{for } (|\bar{M}| - |\hat{M}| < M_{th})$$

$$\text{and } (|\bar{M}| + |\hat{M}| > M_{th})$$

$$\text{and } (|\hat{M}| - |\bar{M}| < M_{th})$$

$$\text{where } \theta_1 = \sin^{-1}\left[(M_{th} - |\bar{M}|)/|\hat{M}|\right]$$

In region D:

$$\frac{\hat{\mu}_1}{\hat{M}} = \frac{2}{\pi|\hat{M}|}\left[(|\bar{M}| - M_{th})\cos\theta_1 + \frac{|\hat{M}|}{4}(\pi - 2\theta_1 + \sin(2\theta_1)\right]\frac{\bar{M}}{|\bar{M}|}$$

$$+ \frac{2}{\pi|\hat{M}|}\left[(|\bar{M}| + M_{th})\cos\theta_2 - \frac{|\hat{M}|}{4}(\pi - 2\theta_2 + \sin(2\theta_2)\right]\frac{\bar{M}}{|\bar{M}|} \quad (31)$$

for $(|\hat{M}| - |\bar{M}| > M_{th})$

$$\theta_1 = \sin^{-1}\left[(M_{th} - |\bar{M}|)/|\hat{M}|\right]$$

$$\theta_2 = \sin^{-1}\left[(M_{th} + |\bar{M}|)/|\hat{M}|\right]$$

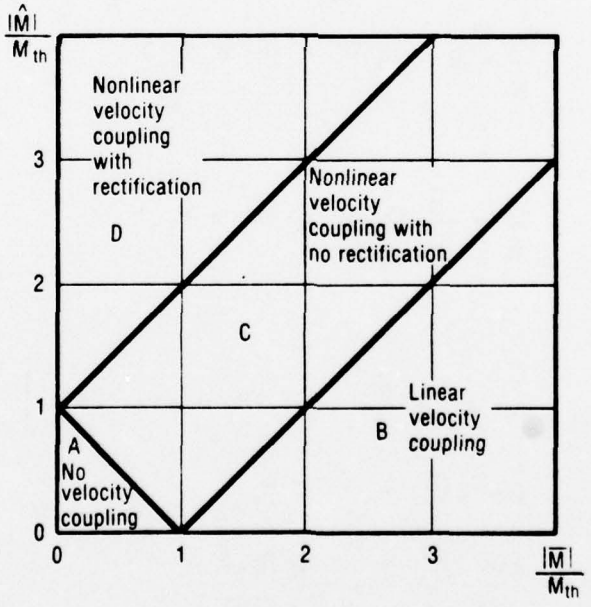

Figure 2-6. Domain of Various Types of Velocity Coupling

21058

These formulas were coded for a digital computer. The validity of the calculations was established by comparing these results with direct computations of the Fourier coefficients from the time domain wave form.

A similar analysis was performed to obtain $\hat{\mu}_o$ and $\hat{\mu}_2$. The $\hat{\mu}_2$ is of interest because it produces a harmonic of the driven frequency and the burner data show significant harmonic content.

In regions A and B:

$$\mu_o = 0 \tag{32}$$

In region C:

$$\mu_o = \frac{\bar{M} - M_{th}}{2} - \frac{(\bar{M} - M_{th})\,\theta_1}{\pi} + \frac{|\hat{M}|}{\pi}\cos\theta_1 \tag{33}$$

$$\theta_1 = \sin^{-1}\left[\frac{M_{th} - |\bar{M}|}{|\hat{M}|}\right]$$

$$\text{if } |\bar{M}| > M_{th}\ \mu_o = \mu_o - (|\bar{M}| - M_{th})$$

In region D:

$$\mu_o = \frac{\bar{M} - M_{th}}{2} - \frac{(\bar{M} - M_{th})\,\theta_1}{\pi} + \frac{|\hat{M}|}{\pi}\cos\theta_1 - \frac{(|\bar{M}| + M_{th})}{2} + \frac{(|\bar{M}| + M_{th})\,\theta_2}{\pi} + \frac{|\hat{M}|}{\pi}\cos\theta_2 \tag{34}$$

$$\theta_1 = \sin^{-1}\left[\frac{M_{th} - |\bar{M}|}{|\hat{M}|}\right]$$

$$\theta_2 = \sin^{-1}\left[\frac{M_{th} + |\bar{M}|}{|\hat{M}|}\right]$$

$$\text{if } |\bar{M}| > M_{th}\ \mu_o = \mu_o - (|\bar{M}| - M_{th})$$

In regions A and B:

$$\hat{\mu}_2 = 0 \tag{35}$$

In region C:

$$\hat{\mu}_2 = \frac{2}{\pi}\left(\frac{M_{th} - |\bar{M}|}{2}\sin 2\theta_1 + \frac{|\hat{M}|}{6}\cos 3\theta_1 - \frac{|\hat{M}|}{2}\cos\theta_1\right) \tag{36}$$

$$\theta_1 = \sin^{-1}\left[\frac{M_{th} - |\bar{M}|}{|\hat{M}|}\right]$$

In region D:

$$\hat{\mu}_2 = \frac{2}{\pi}\left(\frac{M_{th} - |\bar{M}|}{2}\sin 2\theta_1 + \frac{|\bar{M}|}{6}\cos 3\theta_1 - \frac{|\hat{M}|}{2}\cos\theta_1\right) + \frac{2}{\pi}\left(\frac{|\bar{M}| + M_{th}}{2}\sin 2\theta_2 + \frac{|\hat{M}|}{6}\cos 3\theta_2 - \frac{|\hat{M}|}{2}\cos\theta_2\right) \tag{37}$$

$$\theta_1 = \sin^{-1}\left(\frac{M_{th} - |\bar{M}|}{|\hat{M}|}\right)$$

$$\theta_2 = \sin^{-1}\left(\frac{M_{th} + |\bar{M}|}{|\hat{M}|}\right)$$

Plots of $\hat{\mu}_1/\hat{M}$ and $\hat{\mu}_2/\hat{M}$ are shown in figures 2-7 and 2-8. The figures show that the fundamental component of the rectified velocity varies almost linearly with $\bar{M}$ for a constant amplitude of the driving velocity oscillation.

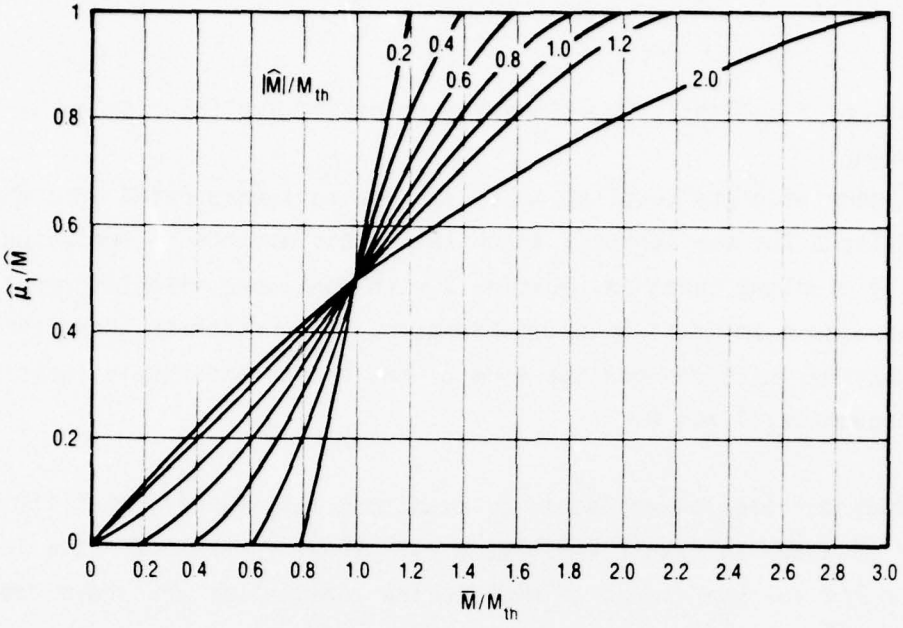

Figure 2-7. Fundamental Component of Speed Threshold

V-10466

21059

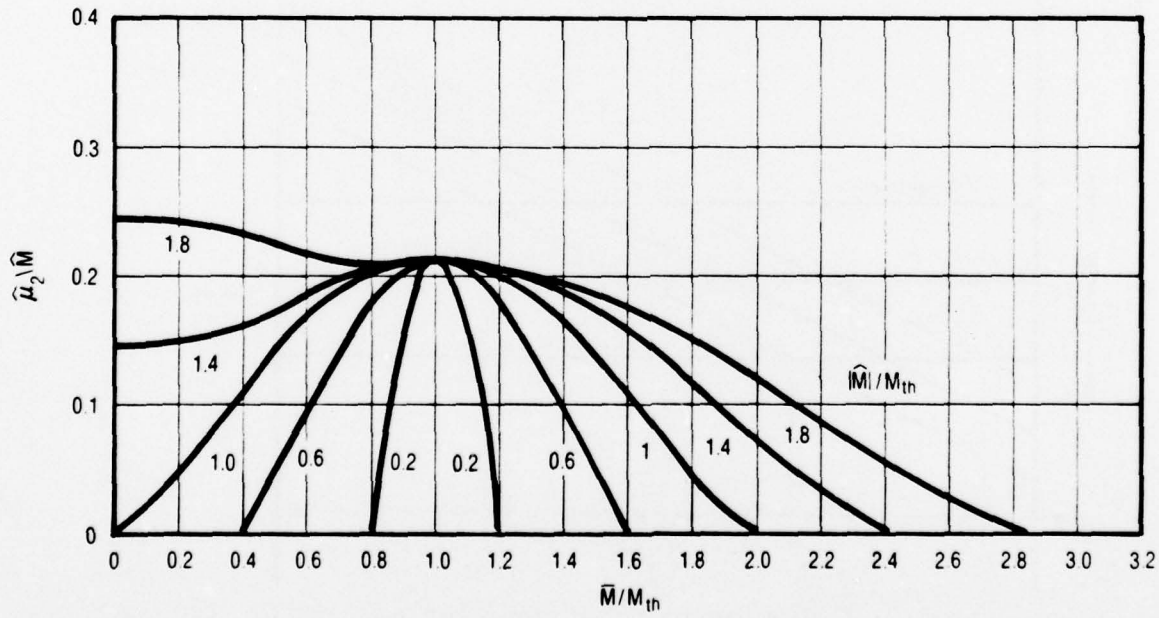

Figure 2-8. Double Frequency Component of Speed Threshold

V-10467

21060

The second component $\hat{\mu}_2$ depends on both $\bar{M}$ and $\hat{M}$ in a manner that is not easily generalized.

2.2.2.2 Solution of Ballistic Equations Incorporating Nonlinear Velocity Coupling

The nonlinear velocity coupling model can now be incorporated into the ballistic equations for the burner. Essentially this amounts to replacing the linear velocity coupling terms in equation 2 with nonlinear velocity coupling terms. This presents an additional complication. The nonlinear terms vary with axial position which changes the form of the second order wave equation derived from equations 1 and 2.

This effect can best be explained by examining the velocity distributions in the burner as shown in figure 2-9. This plot shows $\bar{M}$ versus Z. The locus of the minimum and maximum values of M(Z) during oscillation are shown dotted above and below $\bar{M}$. Two horizontal lines representing the plus and minus thresholds are also shown. The burner is divided into five regions since each

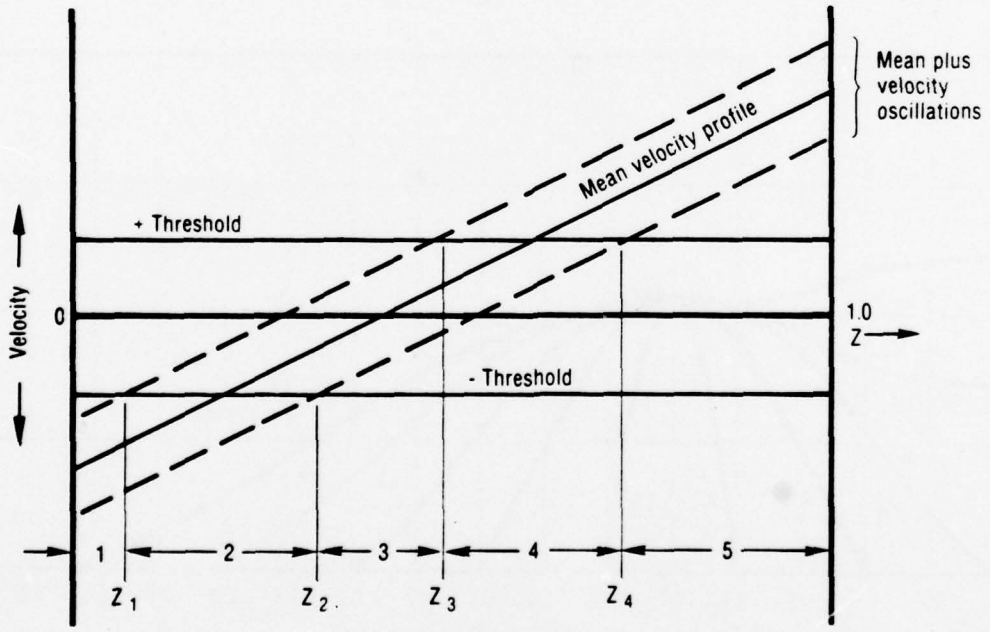

Figure 2-9. Description of Regions Containing Nonlinear Velocity Coupling
V-10464 21061

region has a different formulation for the velocity coupled driving. In regions 1 and 5, linear velocity occurs since the $\bar{M} + M'$ is always greater than the threshold value. In regions 2 and 4 nonlinear velocity coupling occurs, while no response is generated in region 3.

This situation requires the solutions of equations 1 and 2 for each region of the burner. The linear solutions developed in section 2.2.1.1 can be used directly in regions 1 and 5, and in region 3 by setting the velocity response to zero. Regions 2 and 4 are more difficult since both $\hat{M}$ and $\bar{M}$ vary with axial position.

One could always resort to numerical integrations which incorporate these effects at each axial position in regions 2 and 4. However, the basic objective of this analysis is to predict the low frequency behavior; figure 2-7 suggests an approximate approach. At low frequencies, $\hat{M}$ is nearly independent of axial position. Since $\bar{M}$ is linear with axial position, figure 2-7 suggests $\hat{\mu}_1/\hat{M}$ is a linear function of axial position in regions 2 and 4.

By using this approximation, a simple expression for the velocity coupled driving in each of the five regions can be written by redefining the velocity coupled driving term, Y. For nonlinear velocity coupling, Y becomes

$$Y = -\frac{d\bar{M}}{dZ}\,(R_v + \omega_v) \qquad \text{in region 1} \qquad (38)$$

$$Y = -\frac{d\bar{M}}{dZ}\,(R_v + \omega_v)\,K_1\,\frac{Z - Z_2}{Z_1 - Z_2} \qquad \text{in region 2} \qquad (39)$$

$$Y = 0 \qquad \text{in region 3} \qquad (40)$$

$$Y = \frac{d\bar{M}}{dZ}\,(R_v + \omega_v)\,K_4\,\frac{Z - Z_3}{Z_4 - Z_3} \qquad \text{in region 4} \qquad (41)$$

$$Y = \frac{d\bar{M}}{dZ}\,(R_v + \omega_v) \qquad \text{in region 5} \qquad (42)$$

The second order differential equation 11 can be derived if the constants C and N are redefined as

$$2C = \frac{d\bar{M}}{dZ}\left[T_k + Q + 2\frac{d\bar{M}}{dZ} + \frac{1}{Q}\frac{d\bar{M}}{dZ}(R_v + \omega_v)\,G_c\right] + (R_v + \omega_v)\frac{d\bar{M}}{dZ}\,G_c\left[\frac{Q + \frac{d\bar{M}}{dZ}}{Q}\right] \quad (43)$$

$$2N = \bar{\chi}_1\frac{d\bar{M}}{dZ}\left[T_k + Q + 2\frac{d\bar{M}}{dZ} + \frac{1}{Q}\frac{d\bar{M}}{dZ}(R_v + \omega_v)\,G_c\right] + (R_v + \omega_v)\frac{d\bar{M}}{dZ}\,G_n\left[\frac{Q + \frac{d\bar{M}}{dZ}}{Q}\right] \quad (44)$$

where

$$G_c = -K_1/(Z_1 - Z_2) \text{ and } G_n = Z_2 G_c \text{ in region 2} \quad (45)$$

$$G_c = K_4/(Z_4 - Z_3) \text{ and } G_n = Z_3 G_c \text{ in region 4} \quad (46)$$

$$K_1 = \left|\frac{\hat{\mu}_1}{\hat{M}}\right| \text{ at } Z_1 \quad (47)$$

$$K_4 = \left|\frac{\hat{\mu}_1}{\hat{M}}\right| \text{ at } Z_4 \quad (48)$$

The constants, K_1 and K_4, are 1 if regions 1 and 5 exist. There are conditions, however, where these regions do not exist and hence where K_1 or K_4 will be between 0 and 1.

The solution is essentially the same as in section 2.2.1.1, except there are five regions instead of two as in the linear case. Some iteration is required, however, since the locations of the boundaries between regions depend on $\hat{M}(Z)$, which is not known until the final solution is known.

As a first guess, $\hat{M}$ at each end of the burner is calculated from equations 16 and 17 with $\hat{\epsilon} = 0$. Intermediate values are assumed to be linear between the ends. From these estimates of $\hat{M}$, the locations of the region boundaries can be estimated. The solution in each region is defined in terms of the Kummers functions. Equations are written equating $\hat{\epsilon}$ and $\hat{M}$ at the interfaces between the regions together with the boundary conditions for $\hat{\epsilon}$ and $\hat{M}$ at $Z = 0$ and $Z = 1$. A total of 10 linear complex equations and 10 unknowns can be solved to obtain the coefficients D and E in each region. From these coefficients, $\hat{M}$ at the interfaces can be established and new estimates for the locations of the interfaces can be made. This iteration is continued until the changes in the locations of the interfaces are as small as desired. In practice only, one iteration is usually required.

A FORTRAN computer code was written for this analysis on the Burroughs 6700. Besides the normal checking process, cases were run with a zero threshold speed and low amplitude area oscillations. Under these conditions the nonlinear model becomes identical to the linear model (except for the small region where $|\hat{M}| > \bar{M}$. Excellent agreement with the linear model was observed.

A parametric study was then performed assuming the propellant responses followed the thermal lag model. Figures 2-10 through 2-12 show the results for a typical propellant and burner geometry. In figure 2-10 the amplitude of pressure oscillation follows the general trend of decreasing amplitude with frequency expected for the bulk mode. Figure 2-11 shows the ratio of the pressure amplitudes at each end of the burner. The corresponding phase angles are shown in figure 2-12. In the amplitude ratio vs frequency curve, the minimum tends to shift to a lower frequency as the threshold velocity increases. The plot of phase in figure 2-12 shows that the $M_{th} = 0.03$ curve has a different character from the other three curves. For $M_{th} = 0.03$, all the velocities are less than the threshold and no coupling occurs. There is a drastic change from $M_{th} = 0.02$ to 0.03. Additional cases were run to study this change in greater detail. These cases, which are presented in figure 2-13, show that as the amount of velocity coupling approaches zero, the character of the phase curve changes rapidly.

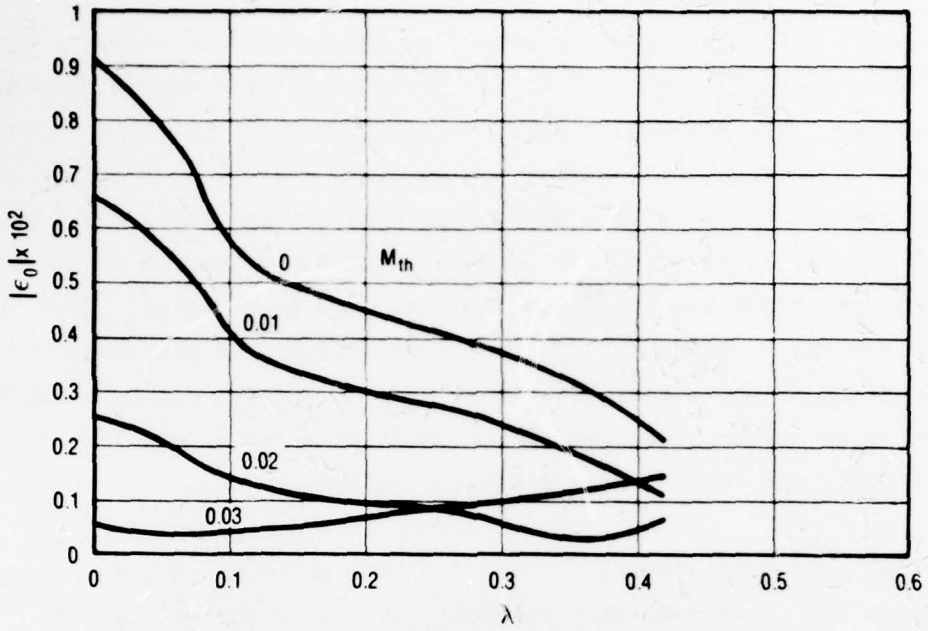

Figure 2-10. Pressure Amplitude from Analytical Model of Velocity-Coupled Rotating Valve (Input Response Based on ANB 3066)

V-10468 21062

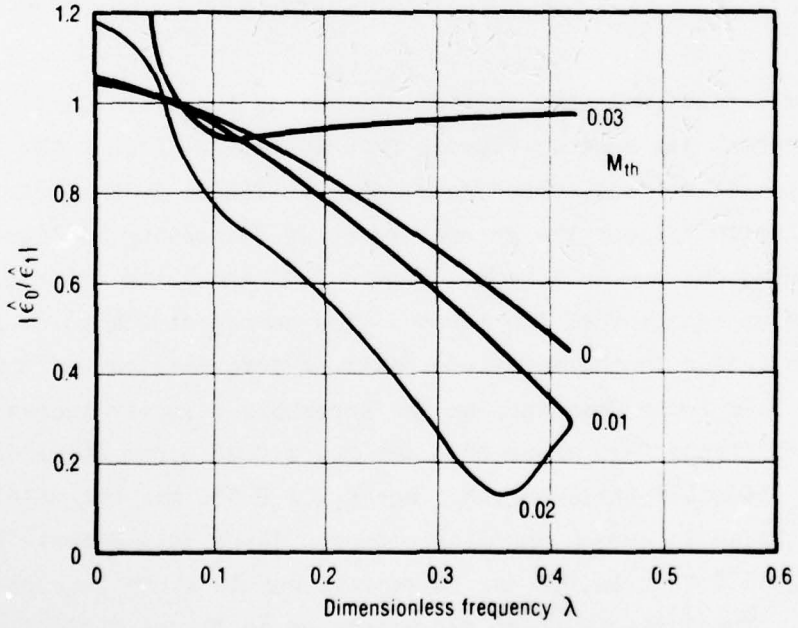

Figure 2-11. Ratio of Pressure Amplitudes (Input Response Based on ANB 3066)

V-10469 21063

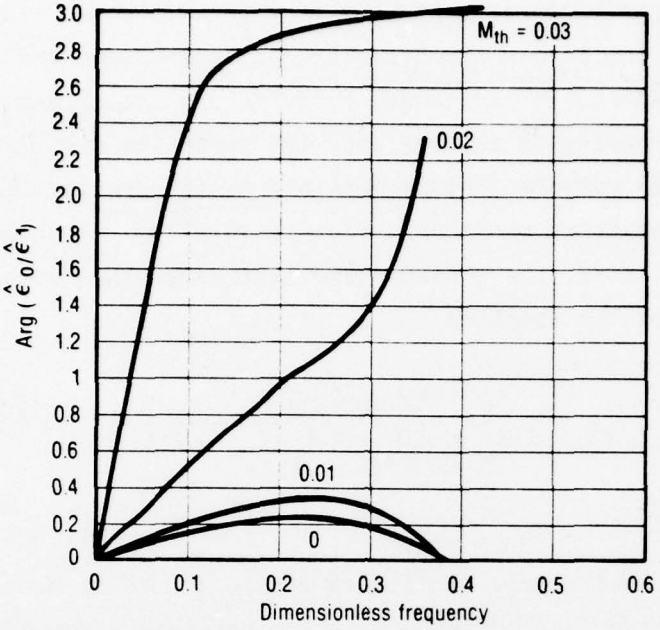

Figure 2-12. Phase of Pressure at Z = 0 to Pressure at Z = 1 (Input Responses Based on ANB 3066) 21064

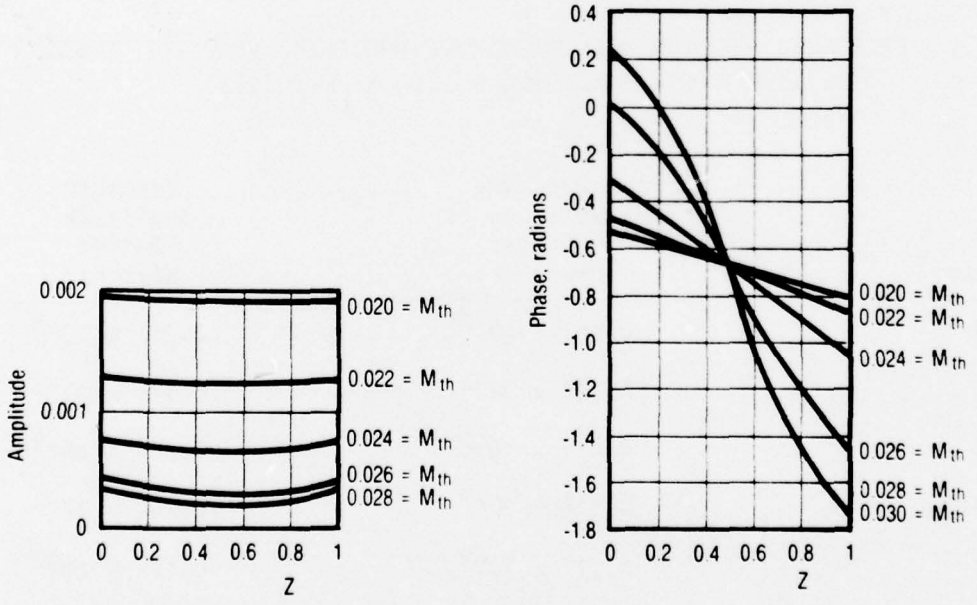

Figure 2-13. Effect of M_{th} on Phase of $\hat{\epsilon}$ vs Z

V-10471 21065

Approximate solutions for amplitude of the pressure oscillations generated at the higher frequency components were also made using this analysis. The oscillations in gas speed can be decomposed into the Fourier components and each component can be assumed to drive the propellant independently. Once the first order solution is obtained, the burn rate oscillation at the double frequency, for example, can be obtained by integrating $(R_v + \omega_v)_{DF}\hat{\mu}_2$ over the regions containing nonlinear velocity coupling. Assuming the burner operates in the bulk mode, the pressure oscillation at the harmonic frequency can be estimated from the equation

$$\hat{\epsilon}_{DF} = \frac{-(R_v + \omega_v)_{DF}\left\langle \hat{\mu}_2 \right\rangle}{\gamma (R_p + \omega_p)_{DF} + \frac{1-3\gamma}{2} - \frac{2i\lambda}{(d\bar{M}/dZ)}} \qquad (49)$$

Estimates for the pressure amplitudes at the second harmonic of the driver frequency were made assuming combustion parameters for ANB 3066. These results are tabulated in table 2-3 below.

TABLE 2-3. PREDICTED PRESSURE AMPLITUDES FOR NONLINEAR VELOCITY COUPLING WITH LINEAR ACOUSTICS (M_{th} = 0.0, $\bar{x}_1$ = 0.1256)

T6195

Driver Frequency	Pressure Amplitude of Driver Frequency	Pressure Amplitude Second Harmonic
0.0598	0.762×10^{-2}	0.367×10^{-3}
0.1197	0.527×10^{-2}	0.346×10^{-3}
0.1795	0.452×10^{-2}	0.314×10^{-3}
0.2394	0.418×10^{-2}	0.202×10^{-3}
0.2992	0.377×10^{-2}	0.123×10^{-3}
0.3590	0.303×10^{-2}	0.81×10^{-4}
0.4189	0.214×10^{-2}	0.59×10^{-4}

These results show that measurable harmonic generation would be produced by nonlinear velocity coupling effects. Since the threshold speed was zero in this case, the harmonics resulted from flow reversal alone. This point will be discussed further in section 2.3.3 when harmonic content of observed pressures are compared to these predictions.

2.2.2.3 Solution for Nonlinear Velocity Response from Measured Pressure Oscillations

The approach to deriving the nonlinear response function, $(R_v + \omega_v)$ from measured pressure oscillations is similar to the approach used in the nonlinear case, section 2.2.1.3. The energy equation for the nonlinear case can be written

$$\frac{d\hat{M}}{dZ} = \left[\frac{d\bar{M}}{dZ}\gamma(R_p + \omega_p) - i\lambda - \gamma\frac{d\bar{M}}{dZ}\right]\hat{\epsilon} - \bar{M}\frac{d\hat{\epsilon}}{dZ} + (R_v + \omega_v)\hat{\mu}_1 \qquad (50)$$

$\hat{M}(Z)$ and $\hat{\epsilon}(Z)$ are assumed to vary linearly with axial position. Hence, the pressure can be defined in terms of the measured pressure at each end of the burner and the flow oscillation can be derived from the transient nozzle flow equations, i.e., equations 13 and 14. Equation 50 can then be integrated to yield

$$\hat{M}(1) - \hat{M}(0) = \int_0^1 \left[\frac{d\bar{M}}{dZ}\gamma(R_p + \omega_p) - i\lambda - \gamma\frac{d\bar{M}}{dZ}\right]\left[\hat{\epsilon}_o + (\hat{\epsilon}_1 - \hat{\epsilon}_o)Z\right]dZ$$
$$- \int_0^1 \frac{d\bar{M}}{dZ}(Z - \bar{X}_1)(\hat{\epsilon}_1 - \hat{\epsilon}_o)\,dZ + (R_v + \omega_v)_{est}\int_0^1 \hat{\mu}_1 dZ \qquad (51)$$

Since $\hat{M}(1)$ and $\hat{M}(0)$ are calculated and $\hat{\epsilon}(0)$ and $\hat{\epsilon}(1)$ are measured, the three integrals can be evaluated and a value can be obtained for $(R_v + \omega_v)_{est}$. In evaluating $\int_0^1 \hat{\mu}_1 dZ$, a linear relationship between $\hat{\mu}_1$ and $\hat{M}$ is assumed for regions 2 and 4.

An effort was made to improve the accuracy of this estimate by using better estimations for $\hat{\epsilon}(Z)$ and $\hat{M}(Z)$. Equation 51 can be used to get a new $\hat{M}(Z)$ by integrating from 0 to Z instead of from 0 to 1. Similarly, the momentum

equation can be used to improve the estimate for $\hat{\epsilon}(Z)$. This equation can be written:

$$\frac{d\hat{\epsilon}}{dZ} = \hat{F} - \hat{\sigma} - \frac{d(\bar{M}\,\hat{M})}{dZ} - i\lambda\hat{M} \qquad (52)$$

With an estimate for $\hat{M}(Z)$ this equation can be integrated to get a new estimate of $\hat{\epsilon}(Z)$. This process could be repeated many times to get better estimates for $(R_v + \omega_v)_{est}$.

This scheme of successive approximation was implemented numerically by dividing the chamber into 50 elements. The method converges rapidly; five decimal place accuracy is achieved within five trials.

The applicability of this inverse solution was examined over a range of conditions by using the forward solution to estimate the pressure oscillation characteristics. In many cases, good agreement was found between the derived and input values for the velocity coupled response function. In other cases, substantial inaccuracies were noted, particularily at frequencies where the magnitude of the velocity response is large. Figure 2-14 shows examples of both results. With lower values of $d\bar{M}/dZ$, good agreement was found while higher values of $d\bar{M}/dZ$ show significant discrepancies.

One possible source for this difficulty is the assumption that $Q \gg \bar{M}Y$ which was carried over from the linear velocity coupling analysis. Parametric studies appear to show that cases when this assumption is valid provide better agreement. Additional study of this point is needed to develop a better understanding of the limitations in this data reduction procedure.

So far, this method has assumed the threshold speed is known. Considerable effort was devoted to the development of a method for deriving this threshold speed from the data. No direct method could be found for deriving the threshold explicitly from the equations. Parametric calculations showed that if several values of M_{th} are used for a given set of $\hat{\epsilon}_o$ and $\hat{\epsilon}_1$, a curve of $Im(R_v + \omega_v)$ versus M_{th} can be drawn. Figure 2-15 shows two such curves for different values of $\bar{x}_1$. In the forward solution, each set of $Im(R_v + \omega_v)$ and M_{th} (for constant $\bar{x}_1$) produces $\hat{\epsilon}(0)$ and $\hat{\epsilon}(1)$ values which are nearly

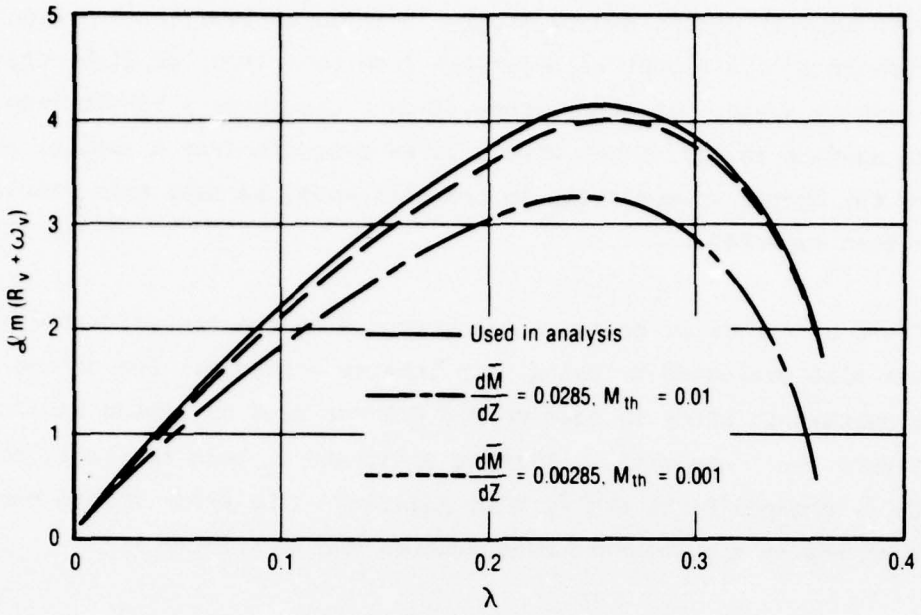

Figure 2-14. Effect of $\frac{d\bar{M}}{dZ}$ on Accuracy of Inversion

21075

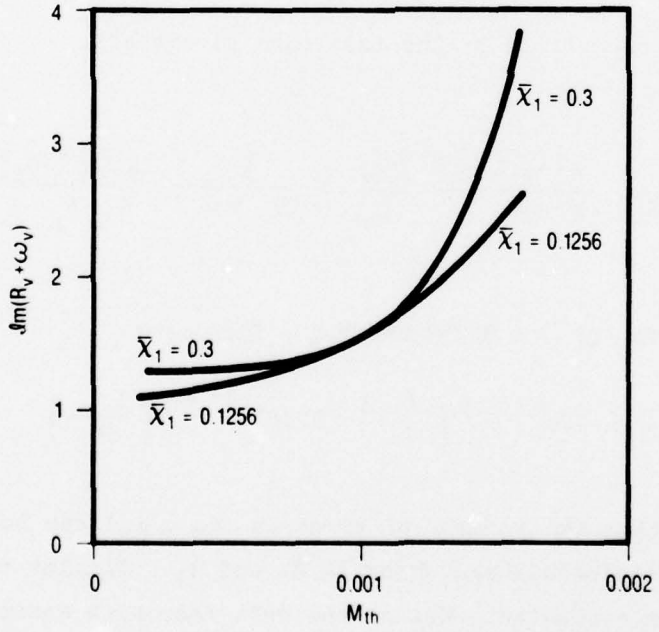

Figure 2-15. Plot of $Im(R_v + \omega_v)$ vs M_{th} for Two Values of $\bar{x}_1$ (True M_{th} = 0.001)

21076

identical. Thus, there is really no unique solution for M_{th} and $Im(R_v + \omega_v)$. Qualitatively, this is equivalent to stating that conditions of low response and low threshold speeds cannot be separated from conditions of high response and high threshold speed. In other words, figure 2-9 shows a little response from a large surface is equivalent with a large response from a smaller surface. Since the burner is operating in the bulk mode, perhaps this result should have been expected.

The effect of errors in pressure measurements on the derived value of $(R_v + \omega_v)$ was also evaluated by using this inverse analysis. One of the cases used in the parametric study in section 2.2.2.2 was used as a base case. Two other cases were run: one with $\hat{\epsilon}_o$ changed by 5% and $\hat{\epsilon}_1$ held constant, and another with $\hat{\epsilon}_1$ changed by 5% and $\hat{\epsilon}_o$ held constant. The error in the response produced by errors in the pressure measurements can be written

$$\Delta (R_v + \omega_v) = \frac{\partial (R_v + \omega_v)}{\partial \hat{\epsilon}_o} \Delta \hat{\epsilon}_o + \frac{\partial (R_v + \omega_v)}{\partial \hat{\epsilon}_1} \Delta \hat{\epsilon}_1 \qquad (53)$$

This equation can be normalized by the base case parameters.

$$\frac{\Delta (R_v + \omega_v)}{(R_v + \omega_v)} = \frac{\hat{\epsilon}_o}{(R_v + \omega_v)} \frac{\partial (R_v + \omega_v)}{\partial \hat{\epsilon}_o} \frac{\Delta \hat{\epsilon}_o}{\hat{\epsilon}_o} + \frac{\hat{\epsilon}_1}{(R_v + \omega_v)} \frac{\partial (R_v + \omega_v)}{\partial \hat{\epsilon}_1} \frac{\Delta \hat{\epsilon}_1}{\hat{\epsilon}_1} \qquad (54)$$

The calculated results for $\lambda = 0.359$ and $M_{th} = 0.01$ are:

$$\frac{\Delta (R_v + \omega_v)}{(R_v + \omega_v)} = 0.52 e^{-i\, 2.97} \left(\frac{\Delta \hat{\epsilon}_o}{\hat{\epsilon}_o} \right) + 0.365 e^{i 3.005} \left(\frac{\Delta \hat{\epsilon}_1}{\hat{\epsilon}_1} \right)$$

This indicates that the percent of error in $(R_v + \omega_v)$ can be expected to be about the sum of the percentage error in $\hat{\epsilon}_o$ and $\hat{\epsilon}_1$. Similar results were found for other cases evaluated. Hence, the data reduction method does not magnify the source of error.

Finally, the effect of errors in the phasing between the area oscillations at the two ends was investigated. Figure 2-16 shows the effect of changes in the phase angle on the amplitude of the pressure oscillation, $|\hat{\epsilon}_1|$. When combined with equation 54 this calculation shows the importance of minimizing errors in phase angle to achieving reasonable accuracy in the derived response.

Significant effort was also devoted an alternative approach for deriving the velocity response from experimental data. This approach is based on Newton's Method. The Kummers function analysis in section 2.2.1.1 calculates $\hat{\epsilon}_o\ (R_p + \omega_p,\ R_v + \omega_v,\ M_{th})$ and $\hat{\epsilon}_1\ (R_p + \omega_p,\ R_v + \omega_v,\ M_{th})$. The effect of small changes in $(R_p + \omega_p)$ and $(R_v + \omega_v)$ on $\hat{\epsilon}_o$ and $\hat{\epsilon}_1$ can be expressed as:

$$d\,\hat{\epsilon}_o = \frac{\partial\ \hat{\epsilon}_o}{\partial (R_p + \omega_p)}\ d\ (R_p + \omega_p) + \frac{\partial\ \hat{\epsilon}_o}{\partial (R_v + \omega_v)}\ d\ (R_v + \omega_v) + \frac{\partial\ \hat{\epsilon}_o}{\partial\ M_{th}}\ dM_{th} \quad (55)$$

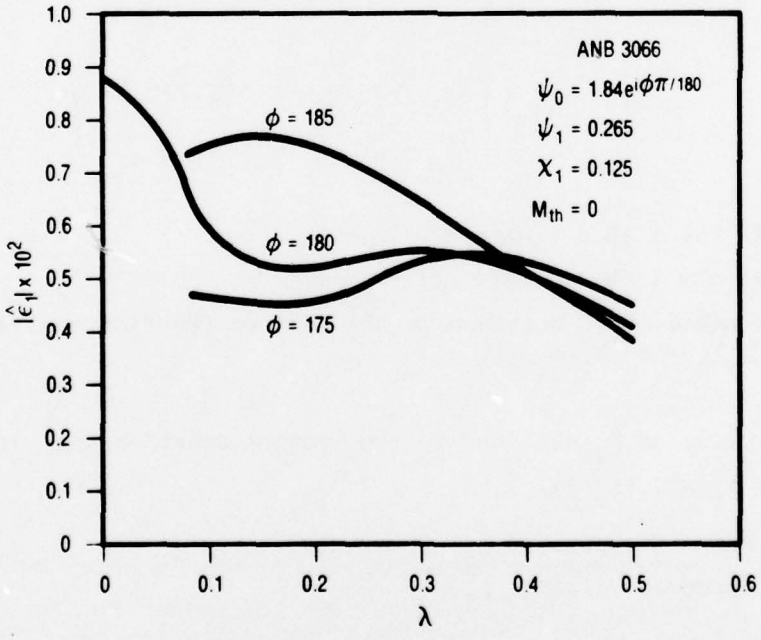

Figure 2-16. Effect of Phasing of Driving on Amplitude of $\hat{\epsilon}_1$

21074

$$d\hat{\epsilon}_1 = \frac{\partial \hat{\epsilon}_1}{\partial (R_p + \omega_p)} d (R_p + \omega_p) + \frac{\partial \hat{\epsilon}_1}{\partial (R_v + \omega_v)} d (R_v + \omega_v) + \frac{\partial \hat{\epsilon}_1}{\partial M_{th}} d M_{th} \quad (56)$$

These equations can be used to set up an iterative procedure for obtaining $(R_p + \omega_p)$ and $(R_v + \omega_v)$ given $\hat{\epsilon}_o$, $\hat{\epsilon}_1$ and M_{th}

$$\hat{\epsilon}_o - \hat{\epsilon}_{oi} = \frac{\partial \hat{\epsilon}_o}{\partial (R_p + \omega_p)} \left[(R_p + \omega_p)_{i+1} - (R_p + \omega_p)_i \right] + \quad (57)$$
$$\frac{\partial \epsilon_o}{\partial (R_v + \omega_v)} \left[(R_v + \omega_v)_{i+1} (R_v + \omega_v)_i \right]$$

$$\hat{\epsilon}_1 - \hat{\epsilon}_{1i} = \frac{\partial \hat{\epsilon}_1}{\partial (R_p + \omega_p)} \left[(R_p + \omega_p)_{i+1} - (R_p + \omega_p)_i \right] + \quad (58)$$
$$\frac{\partial \hat{\epsilon}_1}{\partial (R_v + \omega_v)} \left[(R_v + \omega_v)_{i+1} - (R_v + \omega_v)_i \right]$$

where:

$(R_p + \omega_p)_i$ is the i th estimate of $(R_p + \omega_p)$

$(R_v + \omega_v)_i$ is the i th estimate of $(R_v + \omega_v)$

$\hat{\epsilon}_{oi}$ is the value of $\hat{\epsilon}_o$ obtained in the Kummers function analysis using $(R_p + \omega_p)_i$ and $(R_v^o + \omega_v)_i$

$\hat{\epsilon}_{1i}$ is the value of $\hat{\epsilon}_1$ obtained in the Kummers function analysis using $(R_p + \omega_p)_i$ and $(R_v + \omega_v)_i$

$\hat{\epsilon}_o$ is the measured value of $\hat{\epsilon}_o$

$\hat{\epsilon}_1$ is the measured value of $\hat{\epsilon}_1$

These equations can be used to solve for $(R_p + \omega_p)_{i+1}$ and $(R_v + \omega_v)_{i+1}$. The partial derivatives must be calculated from the analysis by incrementing the independent variables slightly.

$$\frac{\partial \hat{\epsilon}_o}{\partial (R_v + \omega_v)} = \frac{\hat{\epsilon}_o \left[(R_v + \omega_v)_i + \Delta, (R_p + \omega_p) \right] - \hat{\epsilon}_{oi}}{\Delta} \qquad (59)$$

$$\frac{\partial \hat{\epsilon}_o}{\partial (R_p + \omega_p)} = \frac{\hat{\epsilon}_o \left[(R_v + \omega_v)_i , (R_p + \omega_p)_i + \Delta \right] - \hat{\epsilon}_{oi}}{\Delta} \qquad (60)$$

This procedure worked using the $\hat{\epsilon}_o$ and $\hat{\epsilon}_1$ from the forward analysis to recover the values of $(R_p + \omega_p)$ and $(R_v + \omega_v)$, when the value of M_{th} was considered known. However, when studies were made to extend the method to derive values of M_{th}, the method did not converge. Again the basic problem seems to be the inability to separate combustion conditions of low response and low threshold from conditions of high response and high threshold.

A variation of this method was also studied. The amplitude and phase of the pressure oscillation are measured at each end of the burner. With four equations and assuming the real part of $(R_p + \omega_p)$ is known from a single rotating valve test, it should be possible to solve for $Im(R_p + \omega_p)$, $(R_v + \omega_v)$ and M_{th}. This approach was explored but again solutions could not be obtained. Further study showed the equations to be ill-conditioned and development of this approach was terminated.

2.3 EXPERIMENTAL STUDIES

2.3.1 Apparatus Description

A dual rotating valve apparatus was designed and constructed as an integral part of this program. The basic apparatus layout is shown schematically in figure 2-17. Figure 2-18 shows the essential components of the rotating valve in exploded view. The rotor with a graphite sleeve is shown together with four slots in their relative positions. The two slots on the upper left of the picture vent the two auxiliary chambers while those on the lower right vent each end of the combustion chamber. A motor case loaded with propellant is also shown. This arrangement provides the flexibility required to study

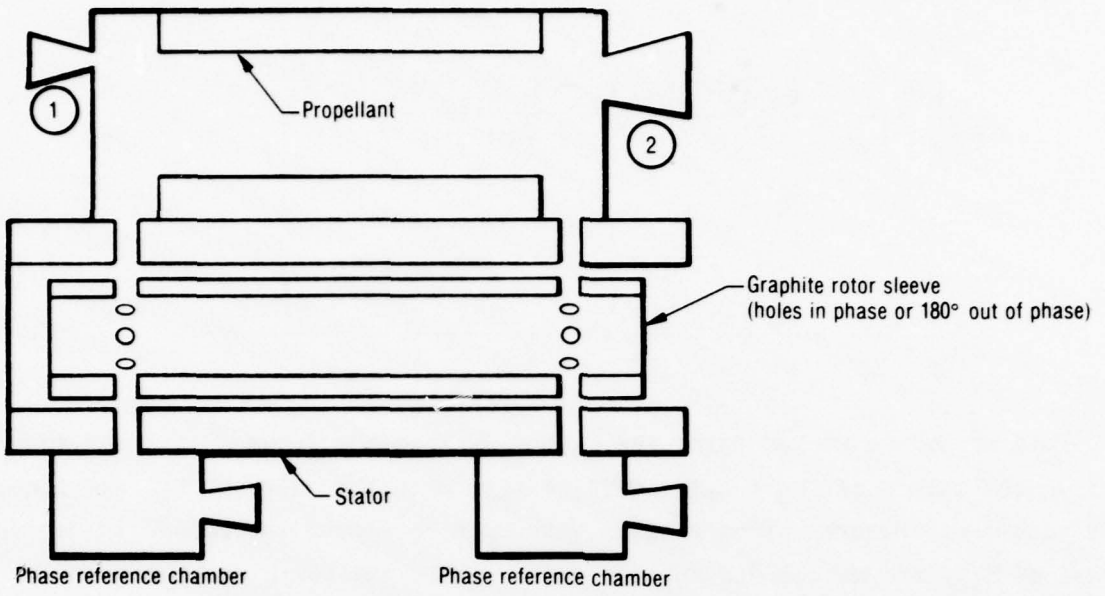

Figure 2-17. Apparatus Layout

08890

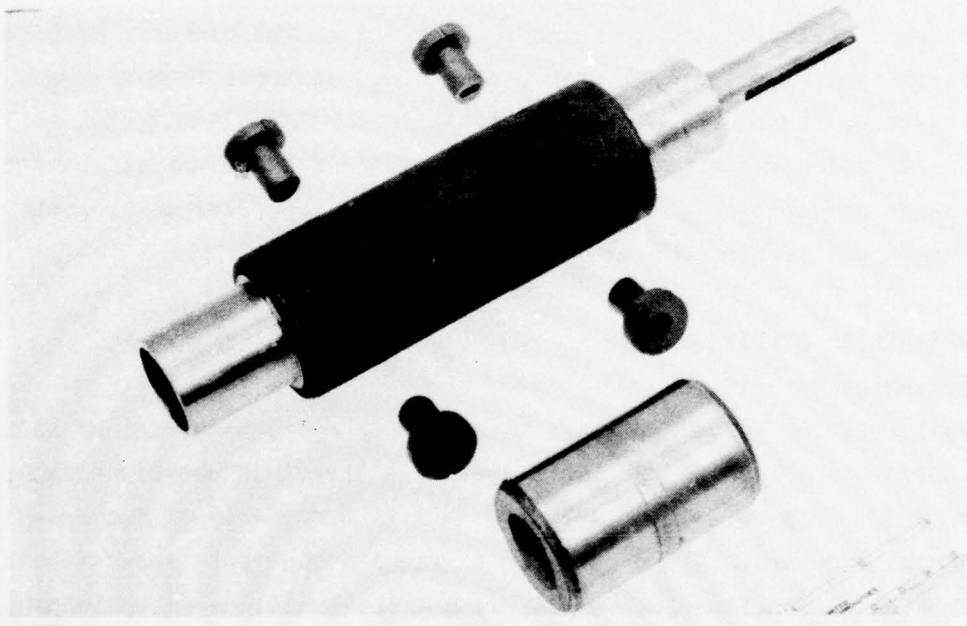

10900-11

Figure 2-18. Dual Rotating Valve Components

12940

both velocity coupled and pressure coupled configurations simply by changing the phase between the two rows of holes in the graphite rotor sleeve.

Experimental studies, which will be described later in this report, demonstrated that the spacing between holes and the relative position of the two rows of holes in the rotor are critical. Essentially the apparatus depends on "phase locking" the two valves together and running the test at a constant frequency. Significant variations in frequency are produced if the holes in each row are not spaced uniformly. The result is significant modulation of the pressure amplitude and substantial errors in the phase angle measurement. Considerable effort was required to define and correct this problem. This aspect of the apparatus represented the major modification from the single rotating valve.

Figure 2-19 shows a photograph of the apparatus with a propellant grain being inserted into the combustion chamber. The steady-state nozzle and igniter wire inserted in preparation for a combustion test are shown in figure 2-20. Kistler pressure transducers are located at each end of the grain to monitor the oscillating component of pressure. In addition, a Taber transducer monitors the average chamber pressure. The valve at each end of the chamber also has an auxiliary chamber which serves as a phase reference. Each is equipped with a Kistler and Taber transducer to monitor the oscillating pressure and the average chamber pressure. All the transducer outputs are recorded with an FM tape recorder and played back through appropriate filters and phase meters as described in references 16 and 17. Figure 2-21 shows the instrumentation facility associated with this apparatus.

The individual slots were calibrated by using the clockwise-counterclockwise rotation procedure developed for the single rotating valve. To calibrate the slot at Z = 0, the vent from the combustion chamber at Z = 1 was plugged. Pressure coupled calibrations were run with the valve rotating in both directions. Comparisons were made with both the auxiliary chambers. This procedure was then repeated with the slot at Z = 0 plugged. Results from these two calibrations were then used to correct for phase differences produced by tolerance build-up.

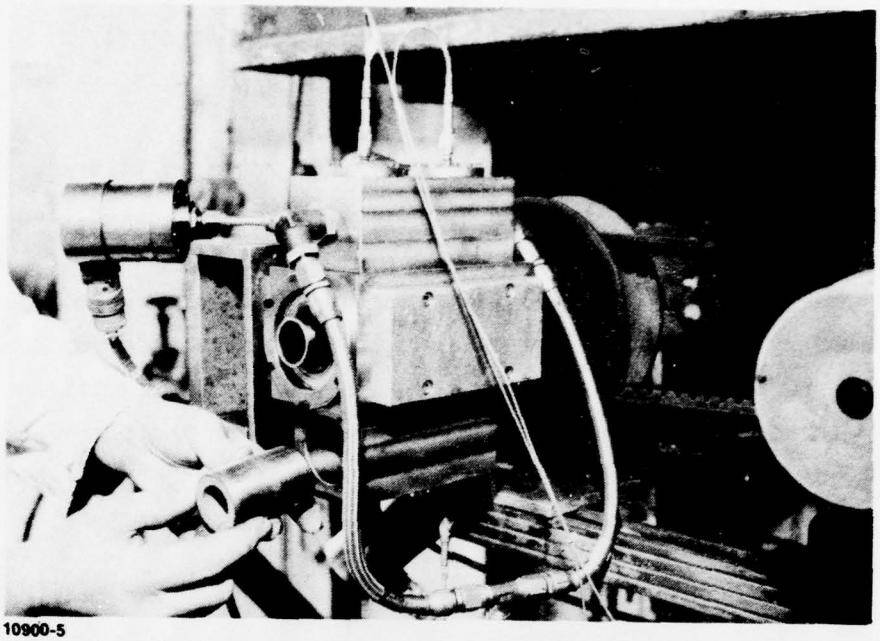

10900-5

Figure 2-19. Propellant Grain and Valve Assembly

12937

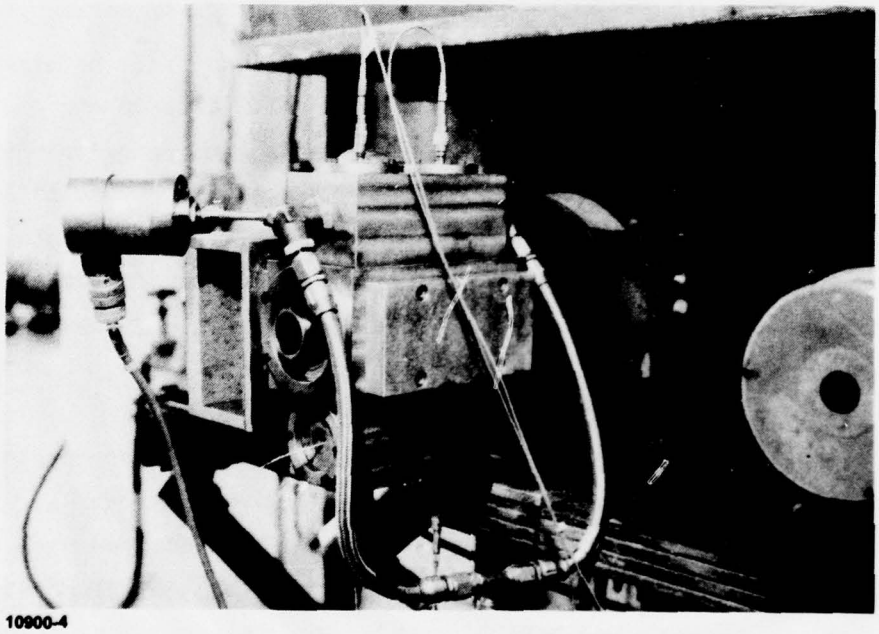

10900-4

Figure 2-20. Assembled Rotating Valve Apparatus

21066

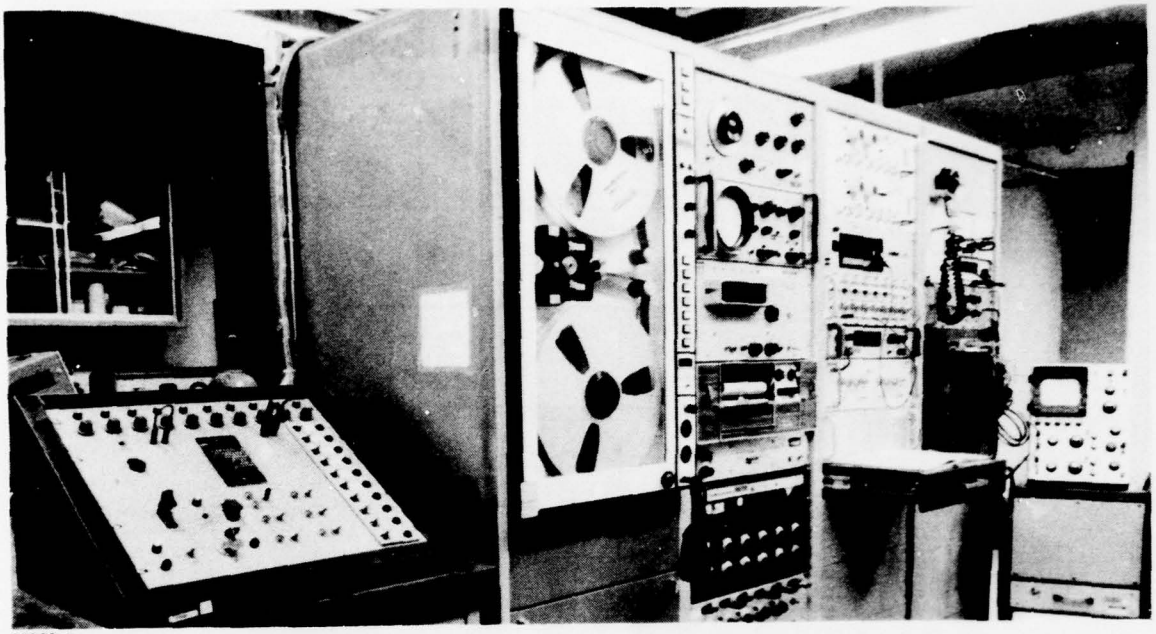

10900-9

Figure 2-21. Instrumentation Facility

21066

2.3.2 Cold-Flow Tests

Cold-flow tests were conducted as the first step in experimentally evaluating this apparatus. In these studies, nitrogen was injected into the combustion chamber and the two auxiliary chambers through individual sonic chokes. The discharge coefficients of all three exhaust nozzles were evaluated by calibration against a standard Venturi flow meter. Under these conditions the response functions are zero and the analysis described in the previous sections can be used to predict the ballistics of all three chambers.

The first series of tests was conducted by using a rotor sleeve where the two rows of holes were in phase, i.e., the pressure coupled configuration. Figure 2-22 shows the excellent agreement obtained between the predicted and observed amplitudes in all three chambers. These tests were conducted at frequencies between 100 and 250 Hz by using the clockwise-counterclockwise method of reference 16.

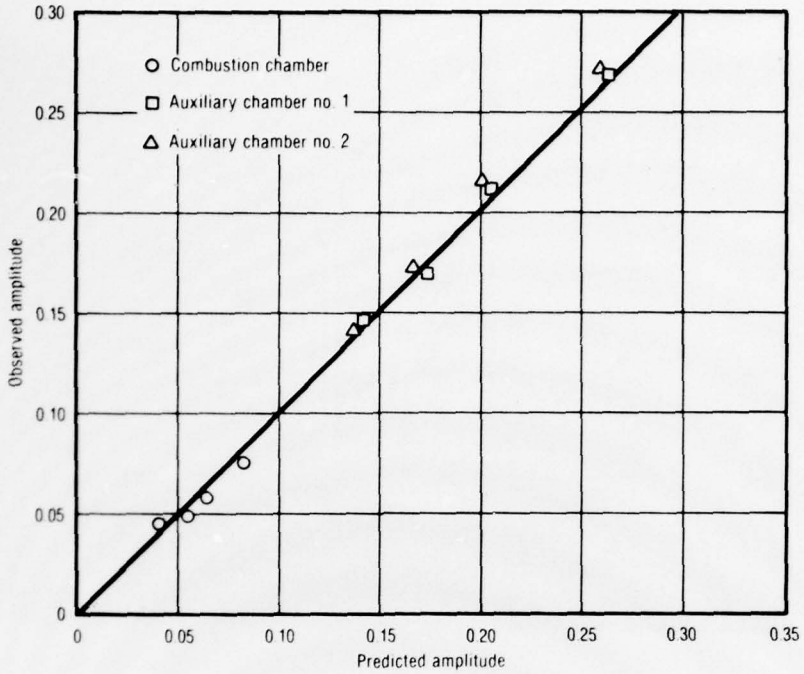

Figure 2-22. Cold-Flow Amplitude Data Pressure-Coupled Dual Valve Configuration

12941

The corresponding phase comparison, shown in figure 2-23, used the oscillating pressure in the combustion chamber as a reference. Again, excellent agreement was obtained between the predicted and observed phase differences. These results are important because they demonstrate that the operation of the apparatus is basically sound when the two valves are operated simultaneously.

These initial tests were conducted by using only one Kistler pressure transducer in the combustion chamber. The analytical studies described in paragraph 2.2, however, showed that pressure measurements at each end of the burner are required. In addition, studies at AFRPL[24] showed that replacing the graphite slots with 90% Ta, 10% W slots increased their service life significantly. Finally, the stainless steel rotor body under the graphite sleeve was replaced with one made from 90% Ta, 10% W to increase the service life. A second series of cold-flow tests was conducted to insure proper operation with these modifications.

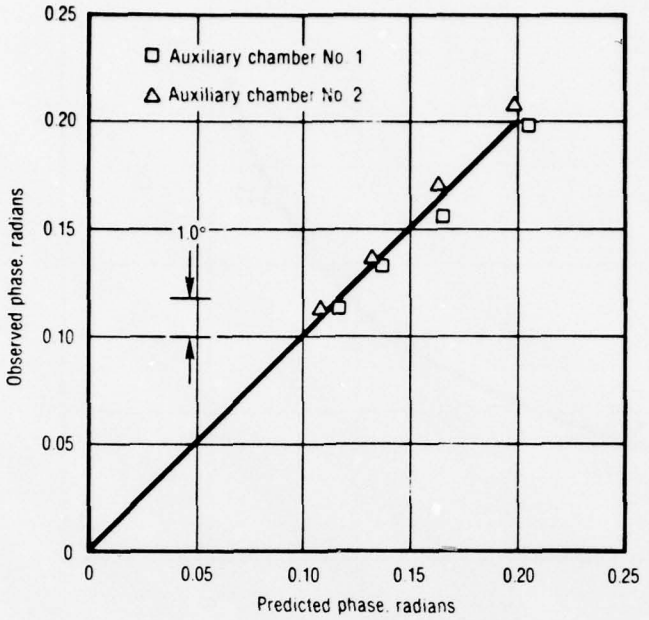

Figure 2-23. Cold-Flow Phase Data, Pressure-Coupled Dual Valve Configuration (Combustion Chamber as Reference)

12942

The results from this second series of tests are shown in figures 2-24 through 2-27. They show excellent agreement between the predicted and measured amplitudes and phase angles. The phase results show little difference when the combustion chamber pressure is measured at each end of the burner. This substantiates the prediction that the burner operates in the bulk mode at these low frequencies. The excellent agreement also substantiates the utility of the clockwise-counterclockwise method for calibrating the individual slot dimensions.

2.3.3 Combustion Tests

The initial combustion tests were conducted to evaluate the performance of the apparatus. The first tests were conducted with the standard rotating valve grains (2.75-in. long by 1.0-in. diameter initial port with a 0.25-in. web) and a steady state nozzle at one end. Figure 2-28 shows oscilloscope pictures of the oscillating pressures at each end of the burner and the mean chamber pressure versus time. The time delay between the rise of P_c and the

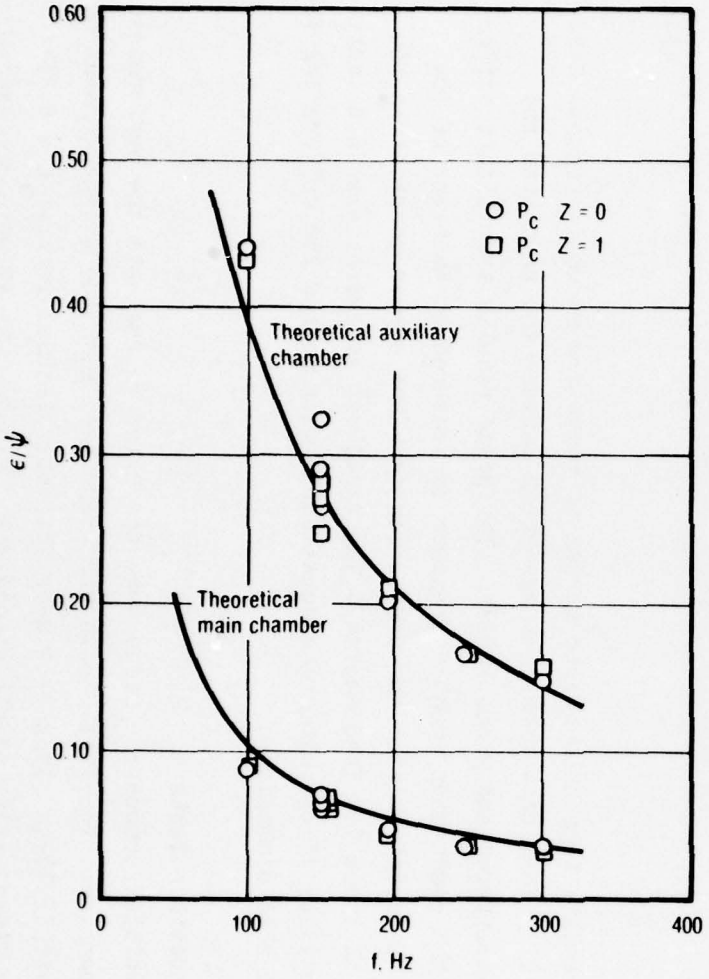

Figure 2-24. Cold Flow with Blocked Vent at Z = 0

15151

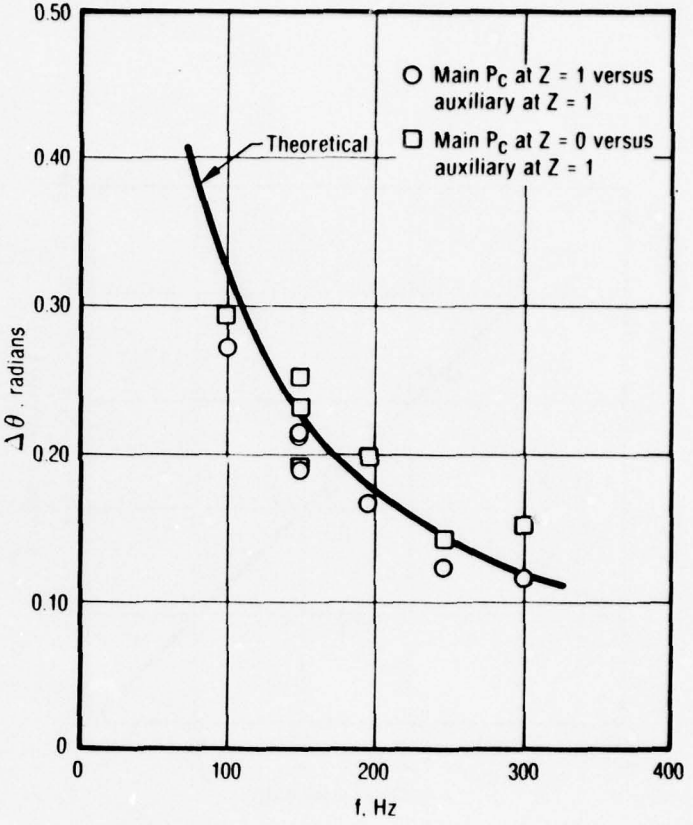

Figure 2-25. Cold Flow with Blocked Vent at Z = 0

15152

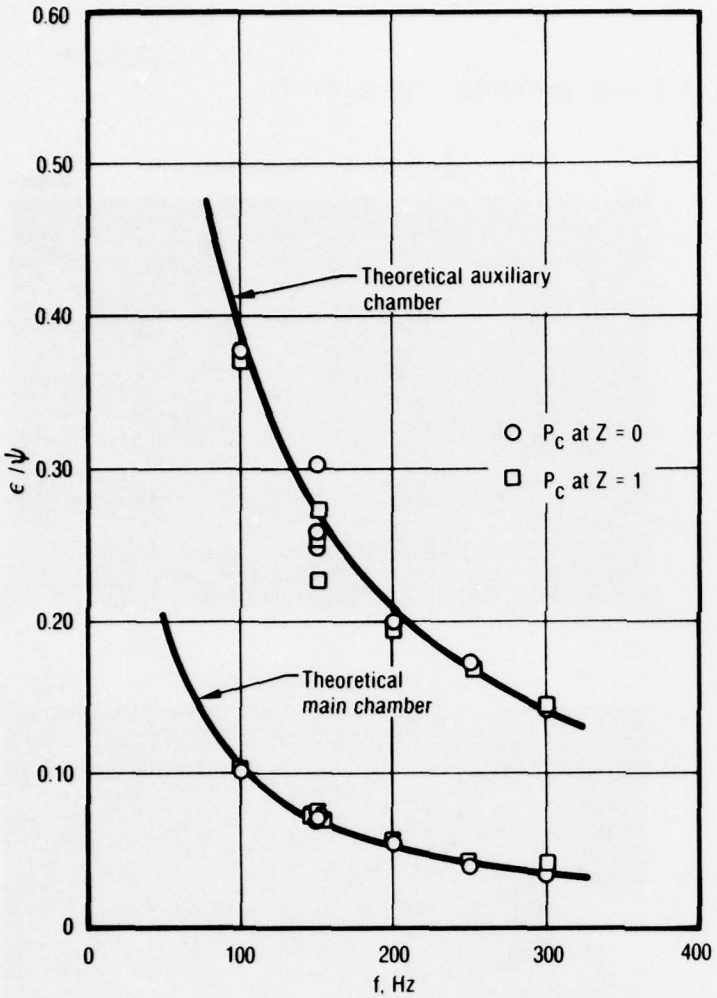

Figure 2-26. Cold-Flow with Blocked Vent at Z = 1

15153

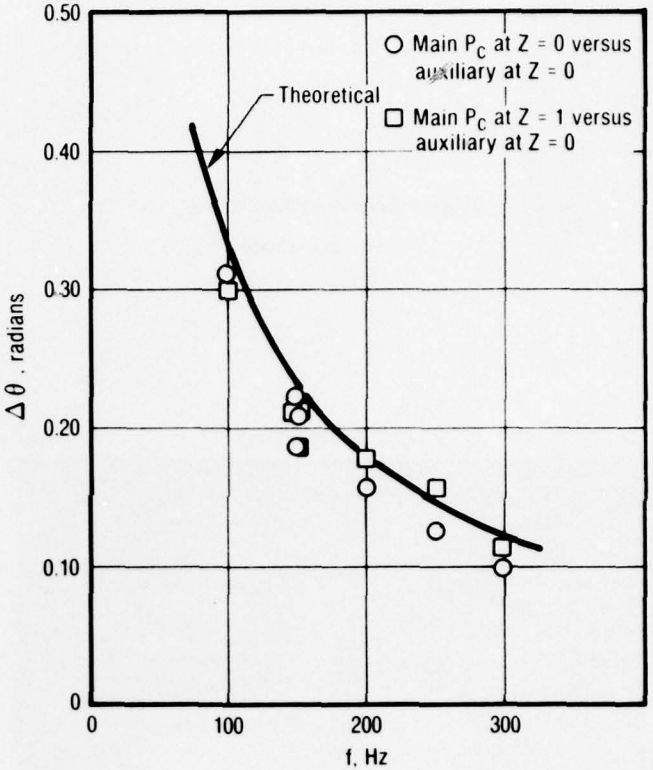

Figure 2-27. Cold-Flow with Blocked Vent at Z = 1

15154

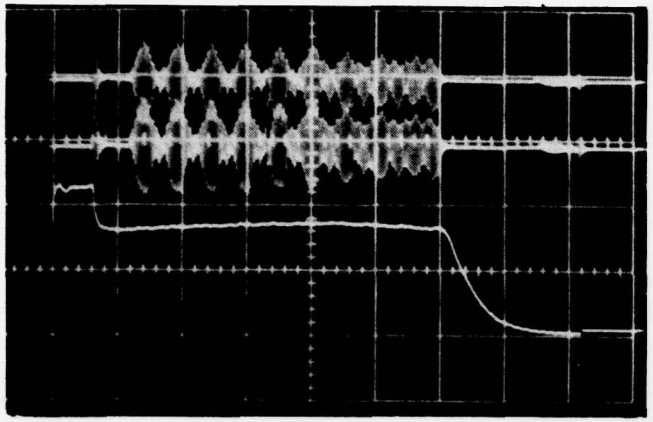

12608-5 Fundamental frequency Q = 4

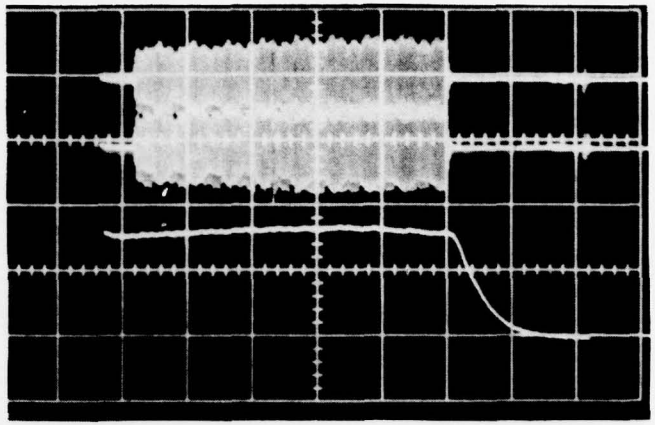

12608-6 Second harmonic Q = 4

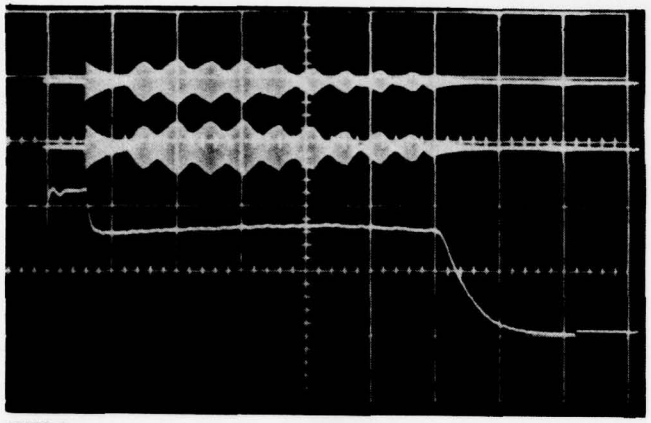

12608-4 Fundamental frequency Q = 64

UTP-19,933

P_{osc} = 2 psi/cm

P_c = 500 psi/cm

Fundamental frequency = 300 Hz

Figure 2-28. Steady-State Nozzle at One End (1-in. Port Diameter)

V-09451

21067

appearance of oscillations resulted from delays in the release of the Kistler grounding circuit. Results are shown for various filter settings, Q, at the fundamental frequency and for the second harmonic content.

The most notable observations are the large amplitude modulations in the oscillating pressure. By imposing the condition that $\partial\hat{\epsilon}/\partial\tau = i\lambda\hat{\epsilon}$, the analysis does not permit evaluation of the modulations. To investigate their source, a series of tests was made using equal steady-state nozzles at each end of the motor. The analysis predicts the amplitude of the oscillations should be extremely small under these conditions. The test results in figure 2-29 show little change from the previous case, which suggests a serious problem in either the apparatus or the analysis.

Further study revealed that the frequency of the modulations is every twenty cycles, which equals the number of holes around the rotor. Careful review of the machining tolerances showed these rotors had minor variations in the circumferential spacing between holes. New rotors were machined to more exacting tolerances. Tests with these new rotors showed a substantial reduction in the magnitude of the modulations, as shown in figure 2-30. Hence, the predominate source of the modulations was the machining tolerances of the graphite rotor sleeves.

Additional combustion tests were then conducted to obtain quantitative velocity coupled combustion response function data. In particular, these tests were made to evaluate the reproducibility of the data and the ability to distinguish differences in propellant formulations. Two nonaluminized formulations and one aluminized formulation were selected. The two nonaluminized formulations, UTP-19,933 and 19,942, were chosen because they had been tested in the T-burner and rotating valve for low frequency pressure coupled response.[25] These data are shown in figure 2-31. More importantly, the high frequency combustion stability properties had been studied in small motor tests. Significant differences in high frequency combustion response were noted between these two formulations, which differ only by the addition of 0.5% of a copper combustion modifier. The burning rates are nearly identical (±10%) for combustion pressures below 1,500 psi. Since high frequency combustion stability

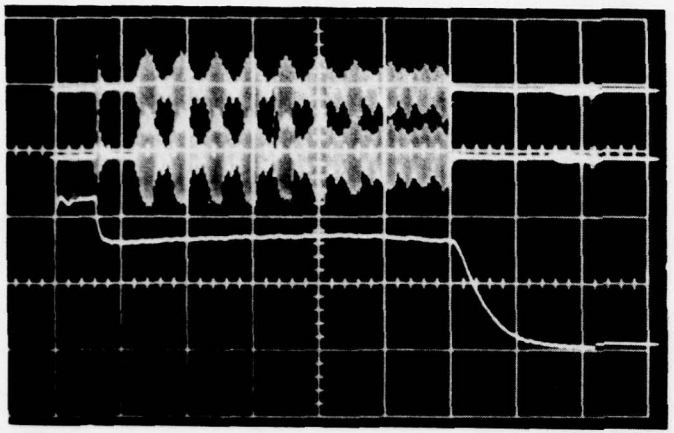

12608-1

Fundamental frequency Q = 4

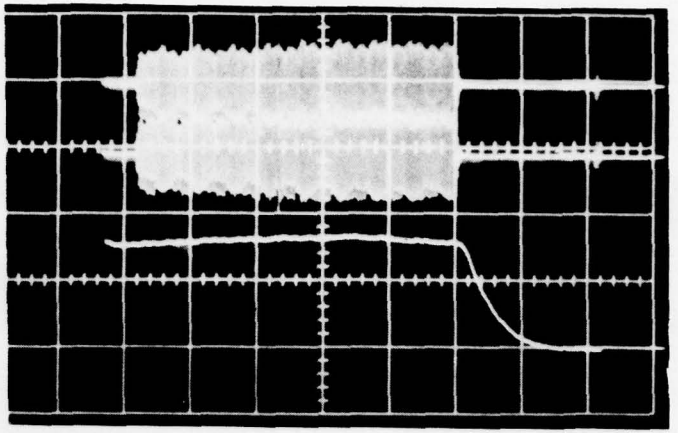

12608-3

Second harmonic Q = 4

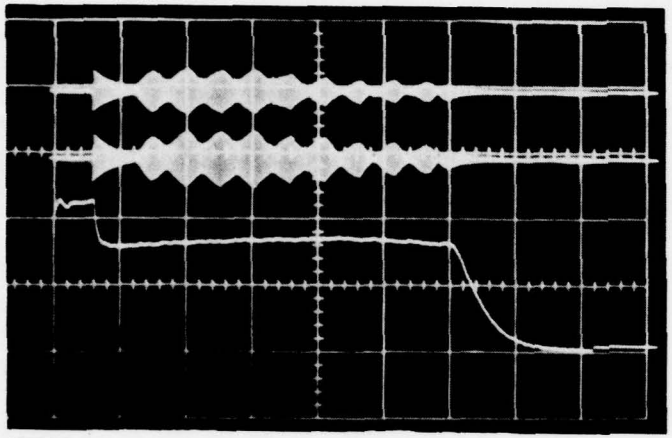

12608-2

Fundamental frequency Q = 64

UTP-19,933

P_{OSC} = 2.0 psi/cm

P_c = 500 psi/cm

Fundamental frequency = 300 Hz

Figure 2-29. Identical Steady-State Nozzles at Each End (1-in. Port Diameter)

V-09453

21068

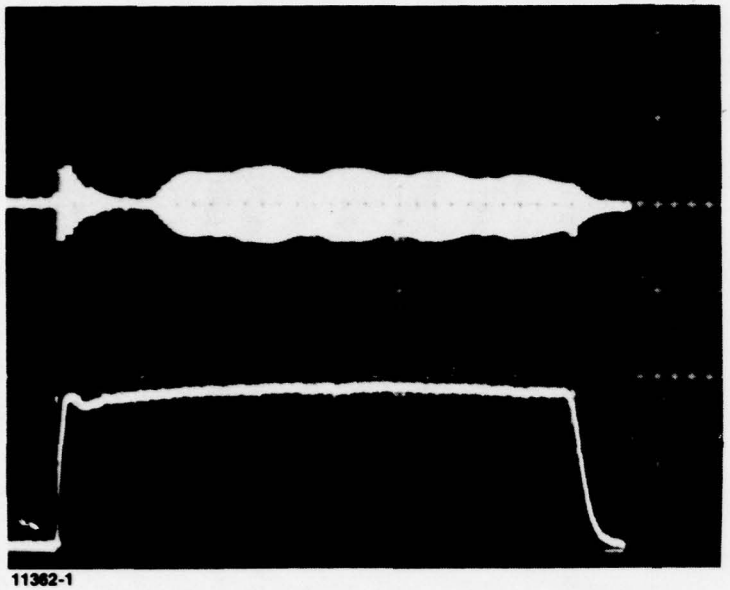

11362-1

1 in. diameter port

P_{osc} = 20 psi/cm

P_c = 400 psi/cm

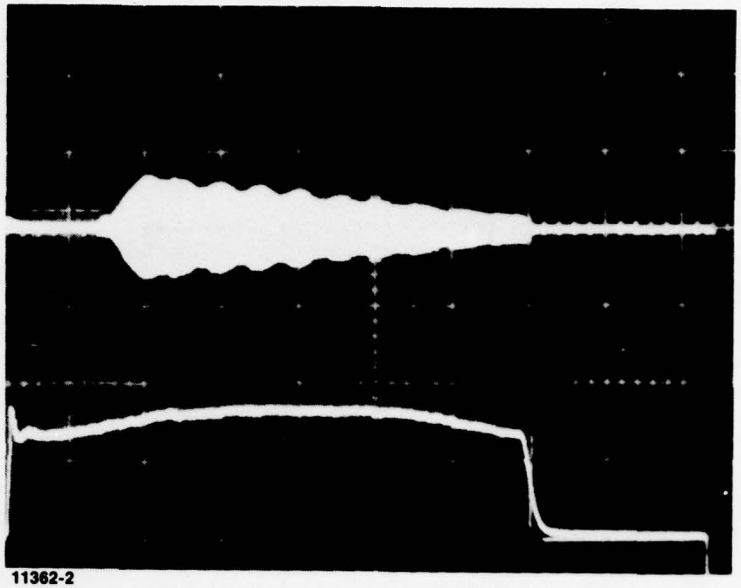

11362-2

0.5 in. diameter port

P_{osc} = 20 psi/cm

P_c = 400 psi/cm

Figure 2-30. Data Using Improved Sleeve (Test Frequency = 150 Hz)

V-10636

21069

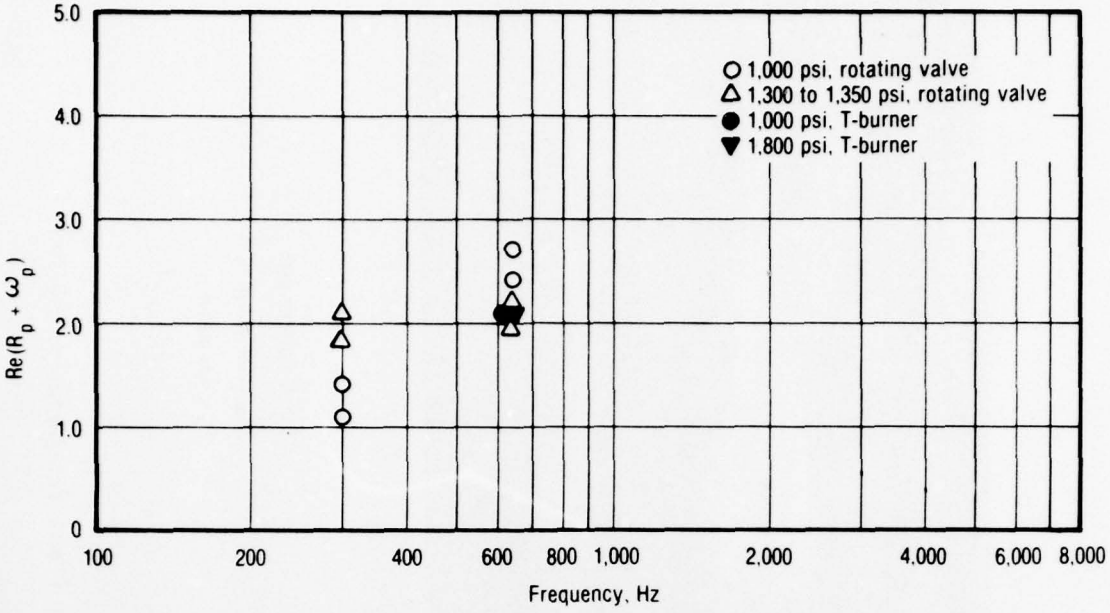

Figure 2-31. Pressure Response Data for UTP-19,933 and UTP-19,942

V-11812 13649

involves gas phase processes, one could argue that perhaps these propellants would also have different velocity coupled responses as well.

Figures 2-32 through 2-34 show the imaginary part of the linear velocity response versus frequency for UTP-19,933, the formulation which does not contain the additive. Since variations in propellant burning rate were noted in these tests, figures 2-33 and 2-34 are attempts to account for these variations in the frequency. In figure 2-33, the frequency has been normalized to the burning rate as suggested by Cohen.[26] In figure 2-34, the frequency has been normalized to the square of the burning rate as suggested by thermal wave combustion models. The imaginary part of the response was selected since this part of the response determines the velocity coupled contribution to combustion stability in motors.

These results show reasonable reproducibility from test-to-test, particularly when one considers the early state of development of this test method and the reproducibility difficulties in the velocity coupled T-burner.

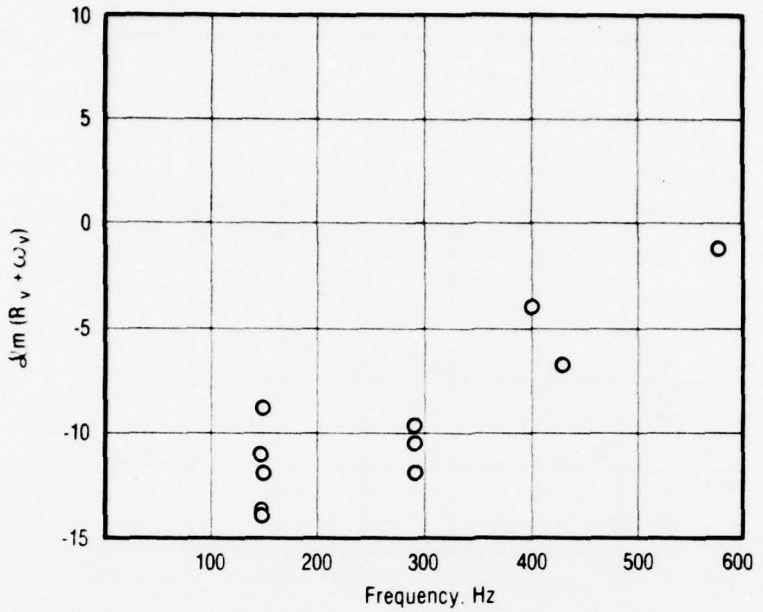

Figure 2-32. Velocity-Coupled Response Function from Dual Rotating Valve Data (UTP-19,933)

21077

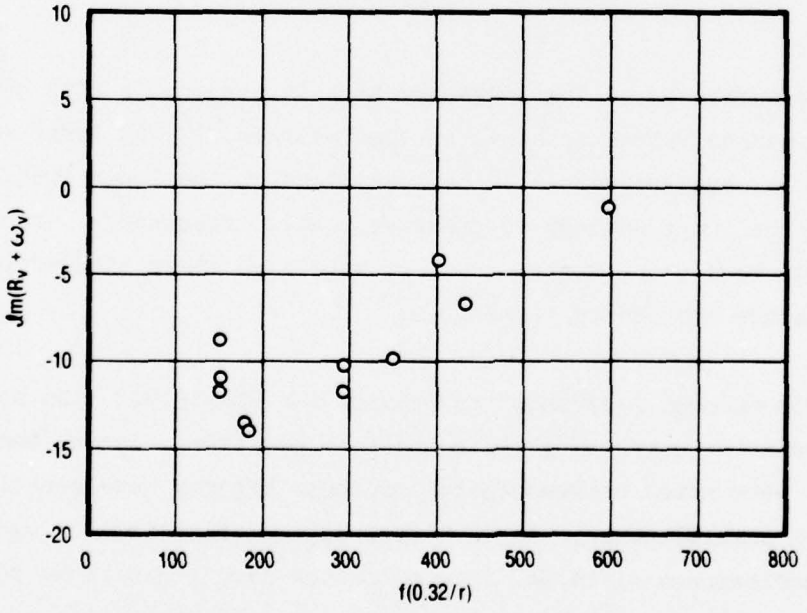

Figure 2-33. Velocity-Coupled Response from Dual Rotating Valve Data (Frequency Corrected by $f(r_o/r)$, UTP-19,933)

21078

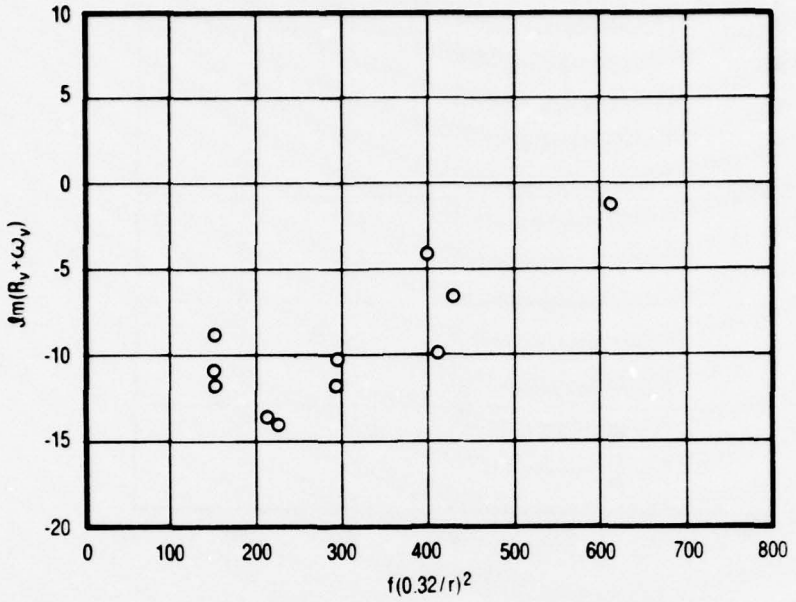

Figure 2-34. Velocity-Coupled Response Function from Dual Rotating Valve Data (Frequency Corrected by $f(r_o/r)^2$, UTP-19,933)

21079

Furthermore, the magnitude of the imaginary part is reasonable when compared to previously reported values obtained in the T-burner.[5,6] At first one might consider the negative values to be suspicious at the lower frequencies, based on the thermal wave analogy to pressure coupled response. T-burner data for nonaluminized propellants, however, have also shown similar behavior, so these results are considered reasonable.

Figures 2-35 through 2-37 show the results for UTP-19,942, the non-aluminized formulation containing the combustion modifier. Again, burning rate variations were noted between tests and these effects have been included in the frequency normalization. Again, reasonable reproducibility was found between tests and between different batches of the same propellant, particularly if one accepts the frequency normalizations and the possibility of multiple peaks in the response. More tests, however, particularly at frequencies between 400 Hz and 600 Hz, are needed to establish these observations more conclusively.

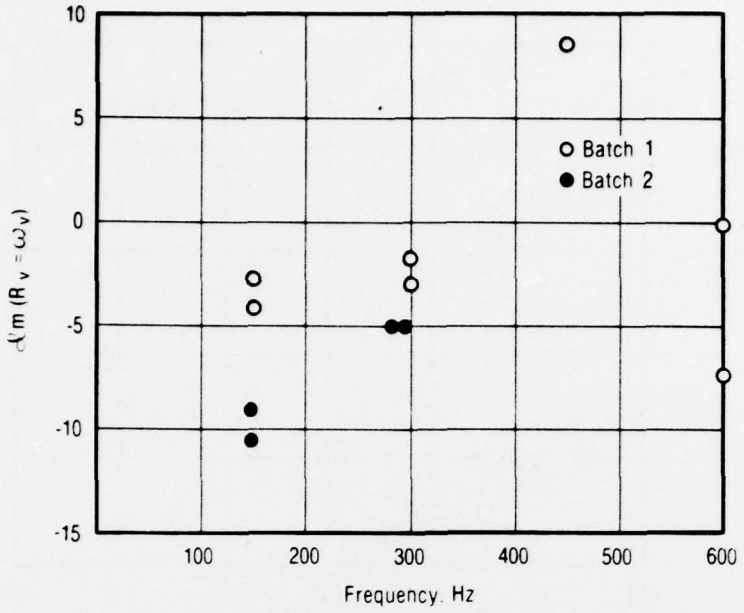

Figure 2-35. Velocity-Coupled Response Function from Dual Rotating Valve Data (UTP-19,942)

21080

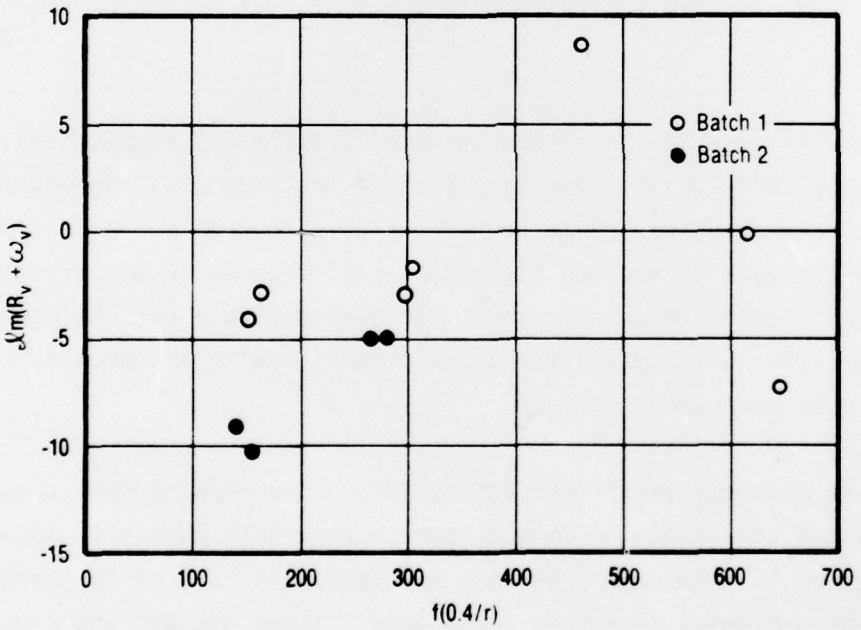

Figure 2-36. Velocity-Coupled Response Function from Dual Rotating Valve Data (Frequency Corrected by $f(r_o/r)$, UTP-19,942)

21081

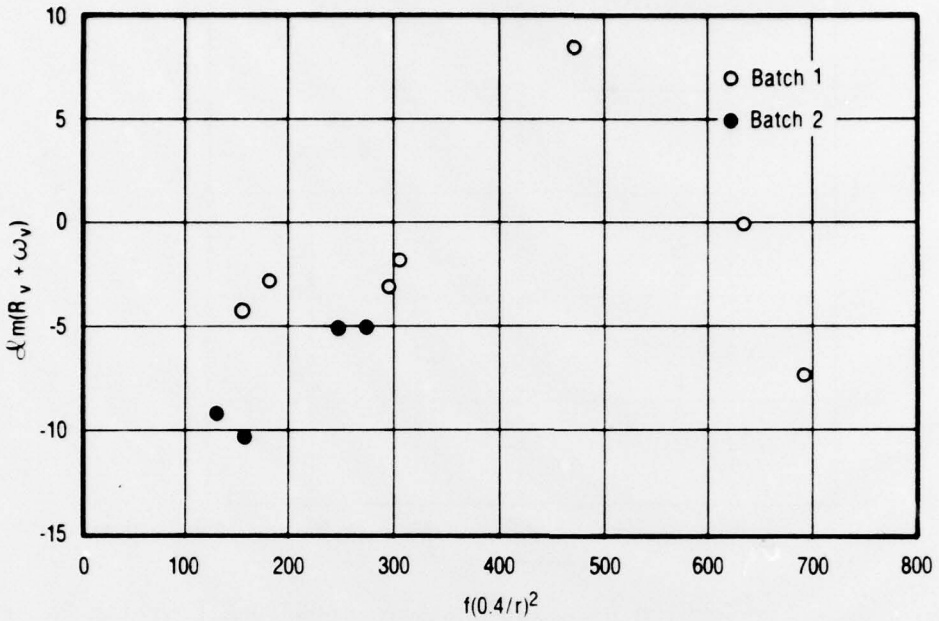

Figure 2-37. Velocity-Coupled Response Function from Dual Rotating Valve Data (Frequency Corrected by $f(r_o/r)^2$, UTP-19,942)

21082

Comparing the results for these two propellants shows significant differences in the magnitude of the imaginary part of the response. In addition, there are important differences in the effect of frequency on the response. This suggests the test method can distinguish differences in propellant formulations and thereby might be useful for qualitatively ranking propellants. Comparisons between rotating valve and motor test results are needed, however, to establish this point conclusively.

Tests were also conducted with UTP-19,360, a low burning rate aluminized propellant, since this class of formulation is generally sensitive to erosive burning. Figures 2-38 through 2-40 show the imaginary part of the response plotted against the three frequency parameters. These results are more difficult to evaluate; one could conclude the scatter is excessive or one could conclude the response is characterized by multiple peaks. In an effort to clarify this point, the pressure response function data from the single rotating valve are shown in figure 2-41. If an analogy between pressure and velocity

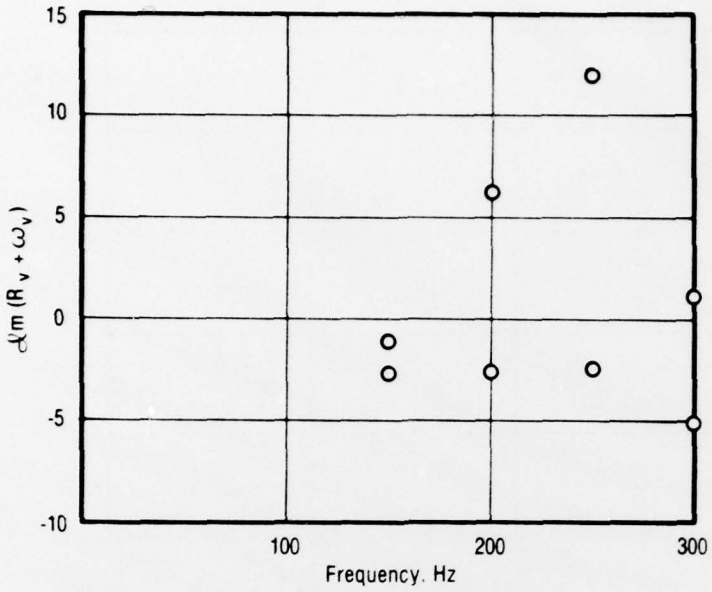

Figure 2-38. Velocity-Coupled Response Function from Dual Rotating Valve Data (UTP-19,360)

21419

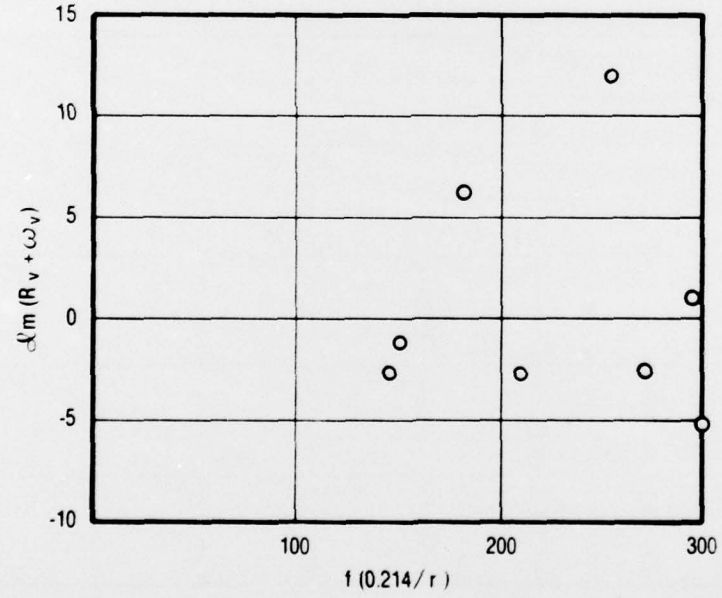

Figure 2-39. Velocity-Coupled Response Function from Dual Rotating Valve Data (Frequency Corrected by $f(r_o/r)$, UTP-19,360)

21420

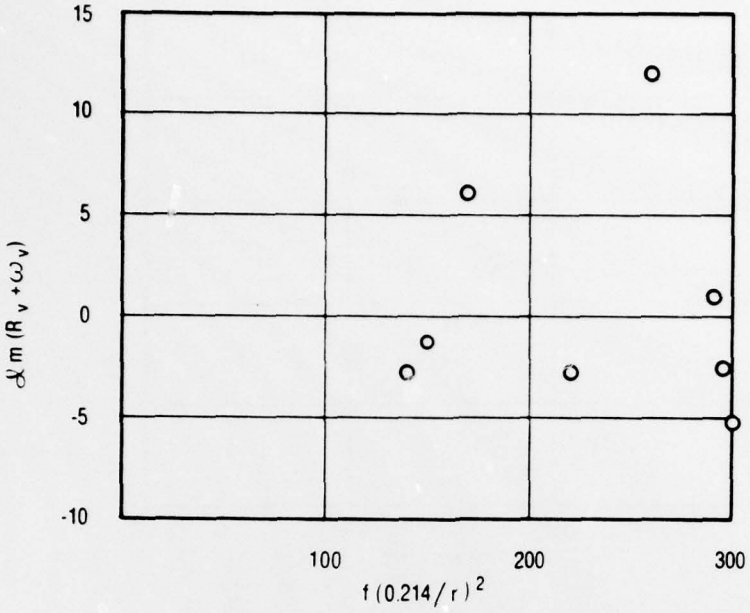

Figure 2-40. Velocity-Coupled Response Function from Dual Rotating Valve Data (Frequency Corrected by $f(r_o/r)^2$, UTP-19,360)

21421

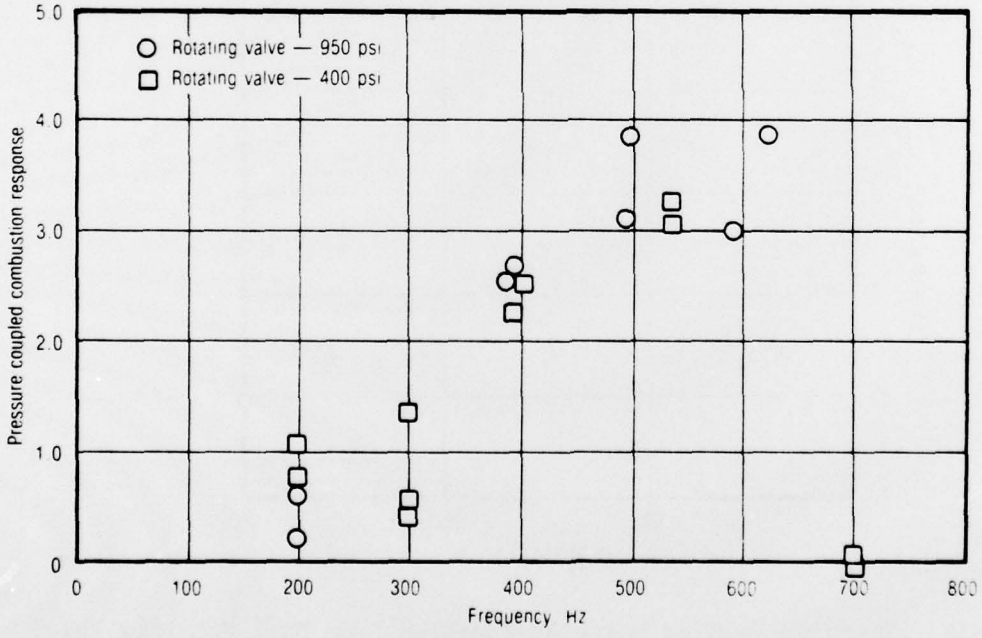

Figure 2-41. Pressure Response Data for UTP-19,360

13787

response can be made from thermal wave arguments, then one would conclude the velocity response exhibits considerable scatter.

Strand, [27] however, has also made pressure response function measurements on this propellant in the microwave bomb. His data, which are shown in figure 2-42, suggest multiple peaks in the pressure response. (They also show a significant difference with the rotating valve data.) This would lead one to suggest the velocity response should also show multiple peaks. Thus, contradictory conclusions can be drawn by following this line of logic as well. This suggests that more work is required to resolve the reproducibility question for this aluminized propellant.

The preceding results were interpreted by using the linear velocity response model. As noted earlier, nonlinear velocity coupling is another possible framework for interpreting velocity response. This model would produce a high harmonic content in the pressure wave; hence, data analyses were conducted to determine the harmonic content of the pressure oscillations. Amplitude spectra analysis from two tests, both conducted at 300 Hz ($\lambda = 0.18$), are shown in figures 2-43 and 2-44. The data shown in figure 2-43 were obtained by using one steady-state nozzle, while the data in figure 2-44 were obtained by using identical steady-state nozzles at each end of the burner. Additional frequency spectra, obtained from a test run at 600 Hz, are shown in fig- 2-45. Several ensembles are shown simultaneously to demonstrate that the spectra are essentially constant during the entire test.

Several observations can be made. First, these figures show significant harmonic content. Analysis of the area wave form[16] shows no driving of the even harmonic by the valve and only minimal (-25 dB) driving of the third harmonic. Thus, the energy at the even harmonics is produced either by the combustion process or by the fluid mechanics of the burner, but not by the rotating valve drivers.

Calculations were then made to determine if nonlinear acoustics or nonlinear velocity coupling could account for this harmonic content. The nonlinear acoustic calculations described in section 2.2.1.4 clearly established

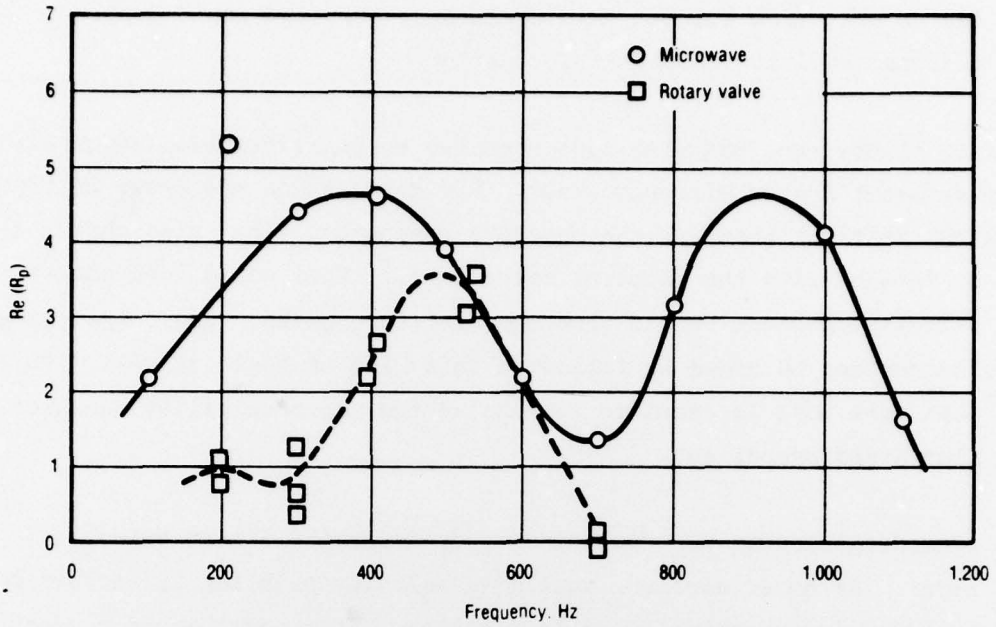

Figure 2-42. Comparison of Response Function vs Frequency Results for UTP-19,360 Propellant Formulation (400 psia Nominal Pressure)

21422

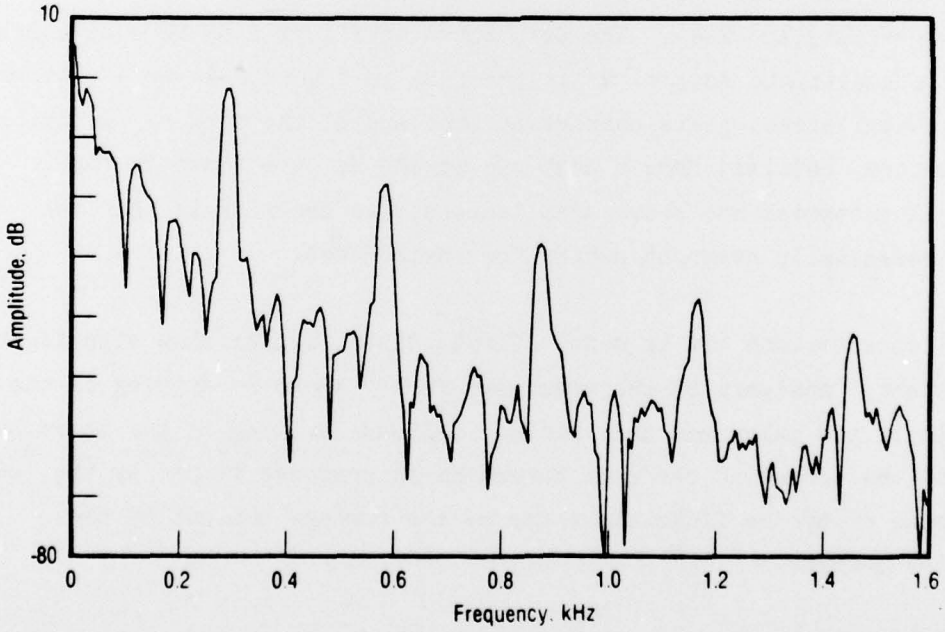

Figure 2-43. Pressure Spectra ($\bar{x}_1$ = 0.1256)

21071

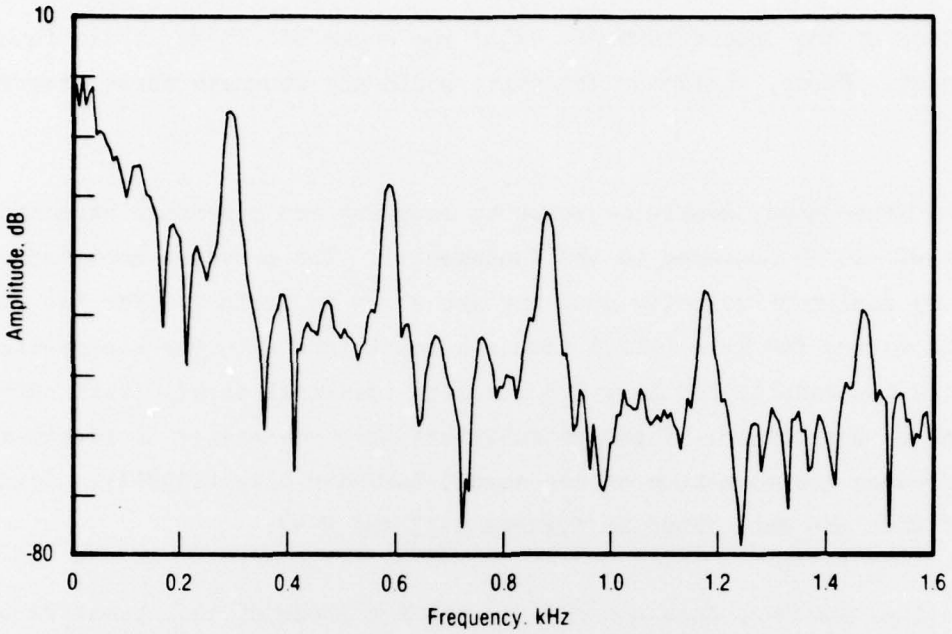

Figure 2-44. Pressure Spectra ($\bar{x}_1 = 0.5$)

21072

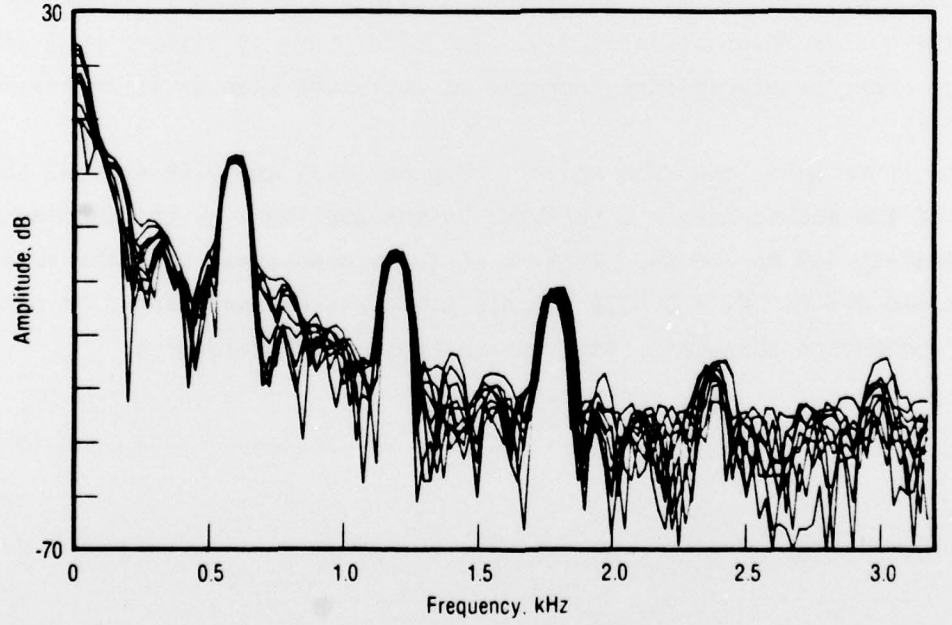

Figure 2-45. Frequency Spectra During Test

21073

the amplitude of the second harmonic is of the order of -55 dB of the fundamental component. Hence, nonlinear acoustics could not generate these observed spectra.

On the other hand, nonlinear velocity coupling could produce harmonic amplitudes of -25 dB compared to the fundamental. The pressure amplitudes generated by nonlinear velocity coupling are shown in table 2-4 for two values of $\bar{X}_1$. The values for $\bar{X}_1 = 0.1256$ simulate conditions with one steady-state nozzle while the results for $\bar{X}_1 = 0.5$ simulate identical steady-state nozzles at each end of the burner. These calculations show the change in steady-state nozzle decreases the magnitude of the second harmonic only slightly. This is consistent with the data shown as figures 2-43 and 2-44.

Table 2-4, however, does not explain the magnitude of the pressure oscillation at the driver frequency shown in figure 2-43 and 2-44. The calculations show the pressure oscillation drops significantly when $\bar{X}_1$ is increased to 0.5. Intuitively, one would expect no pressure oscillations at the fundamental under these conditions. Additional analyses show that momentum effects generate the values shown in table 2-4. The data shown in figures 2-43 and 2-44 do not show the significant decrease in amplitude when $\bar{X}_1$ is increased.

On the other hand, the data shown in figures 2-43 and 2-45 suggest the amplitude of the second harmonic relative to the amplitude at the fundamental is approximately -18 to -20 dB. This is at least consistent with the values shown in table 2-4 for $\bar{X}_1 = 0.1256$. Since table 2-4 was calculated by using estimated combustion responses, this agreement is relatively good.

TABLE 2-4. PREDICTED PRESSURE AMPLITUDES FOR NONLINEAR VELOCITY COUPLING FOR ANB 3066 WITH LINEAR ACOUSTICS (M_{th} = 0.00)

T6196

	$\bar{x}_1$ = 0.1256		$\bar{x}_1$ = 0.5	
Driver Frequency	At Driver Frequency	At Second Harmonic	At Driver Frequency	At Second Harmonic
0.0598	0.762×10^{-2}	0.367×10^{-3}	0.986×10^{-3}	0.432×10^{-3}
0.1197	0.527×10^{-2}	0.346×1^{-3}	0.268×10^{-3}	0.353×10^{-3}
0.1795	0.452×10^{-2}	0.314×10^{-3}	0.606×10^{-3}	0.294×10^{-3}
0.2394	0.418×10^{-2}	0.202×10^{-3}	0.783×10^{-3}	0.184×10^{-3}
0.2992	0.377×10^{-2}	0.123×10^{-3}	0.956×10^{-3}	0.108×10^{-3}
0.3590	0.303×10^{-2}	0.810×10^{-4}	0.113×10^{-2}	0.694×10^{-4}
0.4189	0.214×10^{-2}	0.590×10^{-4}	0.131×10^{-2}	0.505×10^{-4}

3.0 CONCLUSIONS

Two analytical models of the dual rotating valve were developed to estimate the burner performance and derive velocity coupled response functions from experimental data. Both models are based on one-dimensional, linear gas dynamics; one includes a linear velocity coupling model, and the second incorporates an amplitude dependent velocity coupling model. The effects of pressure coupling, flow turning, and particle damping are also included in both models. Parametric and analytical studies demonstrated that the equations predict the proper bulk mode behavior at low frequencies. The analyses also predict the linear damping at the natural acoustic frequencies which agrees with alternative prediction methods. Finally, excellent agreement was demonstrated with the model for the modulated throat rocket motor.

Analytical studies demonstrated the utility of the data reduction methods. For the linear velocity coupling model, the data reduction process was found to introduce a maximum error of ±20%. A typical error, however, was found to be closer to ±10%. Analyzing the data with the nonlinear velocity coupling model was more difficult. If the threshold speed is known independently, these methods provide satisfactory results. Separating the response function from the threshold speed, however, is extremely difficult and as yet no satisfactory method has been developed.

Cold-flow tests confirm the behavior predicted for the pressure coupled configuration at low frequencies. In the velocity coupled configuration, control of the phase angle between the two valves was found to be extremely important. Methods and specifications were developed to achieve the necessary accuracy. Methods for calibrating the mechanical alignment of the apparatus were also demonstrated.

Combustion tests were conducted using both aluminized and nonaluminized propellants. Satisfactory apparatus performance was demonstrated once certain materials were improved and certain design modifications incorporated. Linear velocity response functions were derived for three propellants for frequencies between 150 Hz and 600 Hz. Significant differences in response were found for

these three formulations, thereby demonstrating that the method can distinguish propellant formulation changes. Reasonable reproducibility was found, considering the early status of the development of this test method. Batch to batch reproducibility was also satisfactory at this early stage of development. The frequency of the oscillations was found to be an important parameter. In view of the complexity, nonlinear response functions were not derived from these test data.

Frequency spectra from the pressure oscillations showed significant harmonic content. Estimates for various nonlinear contributions showed the observed harmonic content was 30 dB higher than the contributions from nonlinear gas dynamics. The predicted nonlinear velocity coupling configurations, however, are similar to the observed harmonic content. Hence, these data strongly suggest the nonlinear velocity coupling model predicts some of the qualitative aspects of the data which are observed experimentally. Additional detailed studies are needed, however, to provide additional comparisons before the validity of this model is fully established.

4.0 PUBLICATION CONTAINING RESULTS FROM THIS PROJECT

1. Brown, RS., Willoughby, P.G., and Kelly, V.L., "Rotating Valve for Velocity Coupling Combustion Response Studies," AIAA Paper 77-975 presented at AIAA 13th Propulsion Conference, Orlando, FL, 1977.

2. Brown, R.S., Waugh, R.C., and Kelly, V.L., "Rotating Valve for Velocity Coupling Combustion Response Studies," paper presented at 15th JANNAF Combustion Conference, Newport RI, September 11-15, 1978.

3. Brown, R.S. and Waugh, R.C., "Pressure and Velocity Response Function Measurements by the Rotating Valve Method," paper presented at AGARD 53rd PEP Symposium, Oslo, Norway, April 2-5, 1979.

4. Brown, R.S., Waugh, R.C., and Kelly, V.L. "Rotating Valve for Velocity Coupled Combustion Response Measurements," paper presented at 16th JANNAF Combustion Conference, Monterey CA, September 10-14, 1979.

REFERENCES

1. Eisel, J.L. and Dehority, G.L., "A Technique for Investigating Low Frequency Velocity-Coupled Combustion Instability," CPIA Publication No. 105, Vol. 1, pp. 703-712.

2. Price, E.W. and Dehority, G.L., "Velocity Coupled Axial Mode Combustion Instability in Solid Propellant Rocket Motors," ICRPG/AIAA 2nd Solid Propulsion Conference, June 1967, pp. 213-227.

3. Dehority, G.L., and Price, E.W., "Axial Mode, Intermediate Frequency Combustion Instability in Solid Propellant Rockets," Naval Weapons Center Report NWC-TP-5654, October 1974.

4. Culick, F.E.C., "Stability of Longitudinal Oscillations with Pressure and Velocity Coupling in a Solid Propellant Rocket," Combustion Science and Technology, Volume 2, 1970, pp. 179-201.

5. Beckstead, M.W. and Butcher, A.G., "The Velocity Coupled T-Burner," AIAA Preprint No. 74-200, presented at 13th Aerospace Sciences Meeting, Washington, DC, 1974.

6. Micheli, P.L., "Investigation of Velocity Coupled Combustion Instability," AFRPL Report No. TR-76-100, Aerojet Solid Propulsion Company, 1977.

7. Kruse, R.B., and Glick, R.L., "Velocity-Coupled Instability in Prototype RS MK 36 Motors," paper presented at 16th JANNAF Combustion Conference, Monterey, CA, September 10-14, 1979.

8. Mathes, H.B., "Assessment of Chamber Pressure Oscillations in Shuttle SRB," paper presented at 16th JANNAF Combustion Conference, Monterey, CA, September 10-14, 1979.

9. Beddini, R.A., "A Reacting Turbulent Boundary Layer Approach to Solid Propellant Erosive Burning," AIAA Journal, Vol. 16, September 1978, pp. 898-905.

10. Zucrow, M.J., Osborn, J.R., and Murphy, J.M., "An Experimental Investigation of the Erosive Burning Characteristics of a Nonhomogeneous Solid Propellant," AIAA Preprint 64-107, 1964.

11. Lovine, R.L., Dudley, D.P., and Waugh, R.C., "Standardized Stability Prediction Method for Solid Rocket Motors," AFRPL-TR-76-32, Aerojet Solid Propulsion Company, May 1976.

12. Beckstead, M.W.(Chairman), "Velocity Coupling Workshop," Session at 16th JANNAF Combustion Conference, Monterey, CA, September 10-14, 1979.

13. Culick, F.E.C., "The Stability of One Dimensional Motions in a Rocket Motor," Combustion Science and Technology, Volume 7, 1973, pp. 165-175.

14. Murphy, G.M., Ordinary Differential Equations and Their Solutions, Van Nostrand Reinhold Company, New York, 1960, pp. 323.

15. Abramowitz, M. and Stegan, I.A., "Handbook of Mathematical Functions with Formulas, Graphs, and Mathematical Tables," National Bureau of Standards Applied Mathematics Series No. 55, 1964.

16. Brown, R.S., Erickson, J.E., and Babcock, W.R., "Combustion Response Function Measurements by the Rotating Valve Method," AIAA Journal, Volume 12, 1974, pp. 1,502-1,510.

17. Brown, R.S., "Development and Evaluation of Rotating Valve Combustion Response Test Techniques," AFRPL-TR-75-72, October 1976.

18. Micci, M.M., Caveny, L.H., and Sirignano, W.A., "Linear Analysis of Forced Longitudinal Waves in Rocket Motor Chambers," AIAA Preprint 79-1210, 15th Joint Propulsion Conference, Las Vegas, Nev, June 18-20, 1979.

19. Brown, R.S., and Muzzy, R.J., "Linear and Nonlinear Pressure Coupled Combustion Instability of Solid Propellants," AIAA Journal, Volume 8, 1970, pp. 1,492-1,500.

20. Culick, F.E.C., "A Review of Calculations for Unstable Burning of a Solid Propellant," AIAA Journal, Vol. 6, 1968, pp. 2,241-2,254.

21. Langelle, G., "A Model Describing the Velocity Response of Composite Propellants," AIAA Journal, Vol. 13, 1975, pp. 315-322.

22. Friedly, J.C., and Petersen, E.E., "Influence of Combustion Parameters on Instability at Solid Propellant Motors, Part II, Nonlinear Analysis," AIAA Journal, Vol. 4, 1966, pp. 1,932-1,937.

23. Condon, J.A., "A Model for the Velocity Coupled Response of Composite Propellants," paper presented at 16th JANNAF Combustion Conference, Monterey, CA, September 10-14, 1979.

24. Hewes, J.C., private communication, 1977.

25. Rudy, T.P., Bain, L.S., and Newman, B.D., "Chemical Control of Propellant Combustion," AFRPL-TR-78-15, Chemical Systems Division, April 1978.

26. Cohen, N.S., Taylor, D.E., Small, K.R., Epstein, R.H., Churchill, H.L., "Design of a Smokeless Solid Rocket Motor Emphasizing Combustion Stability," CPIA Publication No. 27 Vol. II, pp. 205-220.

27. Strand, L.D. Private communication, 1979.